First-Principles Approaches to the Structure and Reactivity of Atmospherically Relevant Aqueous Interfaces

Christopher J. Mundy* and I-Feng W. Kuo

Computational Chemistry and Chemical Biology, Chemistry and Materials Science, Lawrence Livermore National Laboratory, PO Box 808, Livermore, CA 94551

Received June 16, 2005

Contents

1. Introduction

The field of atmospheric science is very rich in problems ranging in size from the molecular to the regional and global scale. These problems are often extremely complex, and although the statement of a particular atmospheric science question may be clear, finding a single, concise computational approach to address this question can be daunting. As a result, scientific problems that lie within the umbrella of atmospheric science usually require a multidisciplinary approach. Of particular interest to atmospheric chemists is the role that heterogeneous chemistry plays in the important processes that take place throughout the troposphere and stratosphere. The heterogeneous chemical environment induced by the presence of the interface can differ dramatically from the corresponding gas- or condensed-phase *homogeneous* environment and can give rise to novel chemistry.[1,2] Although the importance of heterogeneous chemistry in the atmosphere has been known for decades,[3,4] a challenge to both experimentalists and theorists is to provide simplified models and experiments that can yield insight into the field measurements of the atmospheric process of interest. Molecular modeling has been widely used to provide a particle-based picture of atmospherically relevant interfaces to deduce novel chemistry that is known to take place. Unfortunately, even with the most computationally efficient particle-based approach, it is still impossible to model the full ice crystal in the stratosphere or the sea-salt aerosol in the troposphere. Figure 1 depicts a caricature of the atmospheric system of interest and highlights the region where efficient molecular modeling can be employed. Although there is seemingly a large disconnect between reality and model, this review will demonstrate that there is still much insight to be gained from a particle-based picture.

There is a myriad of different approaches to molecular modeling that have been successfully applied to studying the complex problems put forth by atmospheric chemists. To date, the majority of the molecular models of atmospherically relevant interfaces have been comprised of two genres of methodology. The first is based on empirical interaction potentials. The use of an empirical interaction potential suffers from at least two shortcomings. First, empirical potentials are usually fit to reproduce bulk thermodynamic states or gas-phase spectroscopic data. Thus, without the explicit inclusion of charge transfer, it is not at all obvious that empirical potentials can faithfully reproduce the structure at a solid−vapor or liquid−vapor interface where charge rearrangement is known to occur (see section 5). One solution to this problem is the empirical inclusion of polarization effects.[5−8] These models are certainly an improvement but still cannot offer insight into charge transfer processes and are usually difficult to parametrize. The other shortcoming of empirical models is that, in general, they cannot describe bond-making/breaking events, that is, chemistry. One exception is the empirical valence bond (EVB) model.[9] This genre of models has been successful in describing proton-transfer reactions in aqueous solutions by capturing the exchange of covalent and hydrogen bonds.[10−12] The advantage of this model is the relatively simple Hamiltonian that can be parametrized by high-level first-principles calculations such as Møller−Plesset perturbation theory (MP2). Furthermore, the inclusion of quantum effects is possible and computationally tractable, and thus EVB methods can be used to study relevant system sizes. Recent formulations of an EVB model also explicitly include polarization effects and thus could be useful in heterogeneous environments.[12] A drawback of such models is that there is some amount of reductionism that is present in the parametrization, often in the form of a postulated reaction coordinate. Because the mechanisms of important atmospheric processes are still unknown, the advantages of an EVB model cannot be fully exploited. However, there are models in the same spirit of the EVB models that incorporate reactivity in terms of a simple Hamiltonian that are directly relevant to results presented in section 4.[13,14]

* Corresponding author. E-mail: mundy2@llnl.gov.

10.1021/cr040375t CCC: $59.00
Published on Web 02/14/2006

Christopher Jay Mundy was born in 1966 in Berkeley, CA. He obtained his B.S. in chemistry at Montana State University in 1988, and went on to obtain his Ph.D. in theoretical chemistry in 1992 at the University of California, Berkeley, with Prof. K. A. Dawson. From 1993 to 1998, he was a postdoctoral fellow at the University of Pennsylvania under the direction of Prof. Michael L. Klein. In 1998, Christopher spent an additional two years as a postdoctoral fellow at the Max-Planck-Institut fuer Festkoerperforschung under the direction of Prof. Michele Parrinello. After 6 months as a member of the technical staff at Sandia National Laboratories in Livermore, CA, Christopher moved to Lawrence Livermore National Laboratory in 2001, where he is presently a group leader in computational chemistry and chemical biology.

I-Feng William Kuo was born in 1974 in Kaoshiung, Taiwan. He obtained his B.S. in Biochemistry at the University of California, San Diego, in 1997 and went on to obtain his Ph.D. in chemistry in 2002 at the University of California, Irvine, with Prof. D. J. Tobias. From 2002 to 2005, he was a postdoctoral fellow at the Lawrence Livermore National Laboratory under the direction of C. J. Mundy. Currently, he is a member of the technical staff at Lawrence Livermore National Laboratory in computational chemistry and chemical biology.

To address novel chemistry, one has to consider an ab initio (to be referred to as first-principles throughout the remaining text) approach to molecular modeling that explicitly utilizes the ground-state electronic wave function to compute forces for the nuclear degrees of freedom. In addition to chemistry, first-principles modeling can also provide a direct link to spectroscopic data (see section 3), but at a large computational cost. The bottleneck associated with first-principles modeling is usually determined by the level of electronic structure theory used to study a particular problem. High-level first-principles approaches, such as MP2, provide an accurate representation of the wave function but are only computationally tractable when applied to small system sizes (i.e., tens of atoms).[15] Nevertheless, this type of modeling has been extremely useful in deducing reaction mechanisms of atmospherically relevant chemistry that will be discussed in this review (see section 4). Moreover, these so-called cluster models of atmospheric reactions have a rich literature relevant to many experimental efforts. When high-level quantum chemistry is applied to small clusters, accurate assignments of the rotational and vibrational spectra can be compared to experiment and thus the ground-state structures of atmospherically relevant moieties can be deduced.[16−23] In turn, these accurate structures and spectroscopic signatures obtained from these static calculations can be used to parametrize accurate empirical models.[21,23] The philosophy here is that if one can capture the correct rotational and vibrational spectroscopy of experimentally characterized water clusters, then in principle, one should have a model that can reproduce bulk phenomena. This approach has been shown to yield a reasonable description of bulk liquid water.[22]

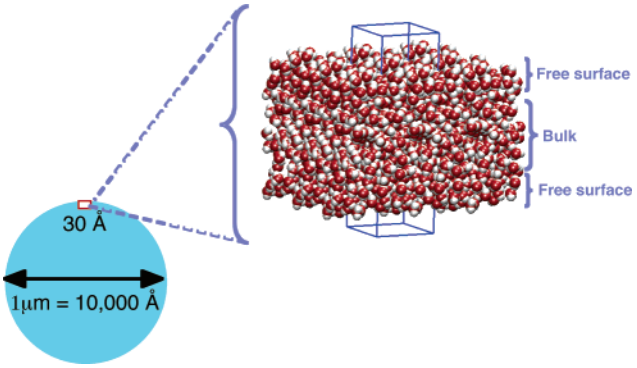

Figure 1. A cartoon depicting the approximations leading to a semi-infinite slab that need to be employed when modeling an aerosol (depicted in aqua) via molecular modeling. Note that the atomistic model of a water interface (oxygen in red; hydrogen in white) of the unreplicated supercell (in blue) is considered a small enough region to be approximately flat. This model also introduces two free interfaces.

Due to the limitation of space, only the first-principles methods that can be utilized to treat the semi-infinite interfacial system, shown in Figure 1, will be discussed. One method that provides a compromise between accuracy and computational efficiency is the Kohn−Sham (KS) formulation of density functional theory (DFT), which will be discussed in section 2. Here, we will review both static and dynamic first-principles methods that provide a direct link to the heterogeneous chemistry that takes place in the troposphere and stratosphere. Within the development of the theory in section 2, we will discuss complementary approaches to the modeling of interfacial systems and the state-of-the-art first-principles simulation protocol for ensuring accurate results for these complicated interfacial systems. Section 3 will focus on the spectroscopic observables that can be directly computed from a first-principles simulation and are relevant to elucidating aqueous systems. Sections 4 and 5 highlight some of the recent work on heterogeneous chemistry on solid−vapor and liquid−vapor interfaces. Last, in section 6, new methodological developments will be previewed that will hopefully lead the reader to conclude that large-scale first-principles modeling of heterogeneous processes has a bright future.

2. Methods

Although there is no strict simulation protocol for the study of heterogeneous systems using first-principles modeling, to obtain experimentally relevant results, there must be a fusion of two components, namely, a fast electronic structure

methodology and an efficient sampling scheme. Both of the aforementioned attributes have been incorporated within the Car−Parrinello approach (CP)[24] to first-principles molecular dynamics (MD). The electronic structure framework of the KS formulation of DFT (KS-DFT) provides the basis for the majority of modern applications to first-principles molecular dynamics.[25−28] The confluence of an orbital-based treatment of the kinetic energy with pure density functional theory[25,26] provides unprecedented computational efficiency over more traditional perturbative methods at the expense of accuracy.[15] Thus, it has been feasible to study bulk materials from first principles for the last four decades. The earliest first-principles MD simulations were performed by quenching the electronic structure to the Born−Oppenheimer (BO) surface at every MD step. The subsequent forces on the ions are a sum of those computed via the Hellmann−Feynman theorem and, in some cases, Pulay forces.[27,29] This method of quenching the wave function at every step of a MD simulation is known as BO MD. Although BO MD is extremely efficient for solids, where the atoms are not significantly diffusing, simulations of liquids via first-principles MD was in need of a more efficient sampling scheme for the electronic degrees of freedom. Furthermore, even with the best wave function optimization schemes, one is not able to efficiently converge to machine precision, thus giving rise to an unwanted drift in the conserved quantity.[30] To cut down on computational cost and increase efficiency and stability of first-principles MD simulation, Car and Parrinello introduced a fictitious dynamics for the electronic degrees of freedom to facilitate on-the-fly computation of the electronic structure.[24]

This on-the-fly sampling of the electronic degrees of freedom is a natural consequence of using an extended Lagrangian that takes advantage of the time-scale separation between the nuclear and electronic degrees of freedom. Thus, the CP extended Lagrangian can be written as[24,30]

$$L_{CP} = \underbrace{\sum_I \tfrac{1}{2} M_I \dot{R}_I^2 + \sum_i \tfrac{1}{2} \mu_i \langle \dot{\psi}_i | \dot{\psi}_i \rangle}_{\text{Kinetic Energy}} - \underbrace{\langle \Psi_0 | H_e | \Psi_0 \rangle}_{\text{Potential Energy}} + \text{constraints} \tag{1}$$

Here, the potential energy is computed from the electronic Hamiltonian, H_e, which will be defined in section 2.1. The total wave function, Ψ_0, is composed of i single-particle orbitals, ψ_i; M_I and R_I denote the mass and position of the Ith ion with the addition of constraints to enforce orthonormality. Kinetic energy for the one-particle orbitals is introduced with fictitious mass μ_i. The equations of motion derived from L_{CP} become

$$\begin{aligned} M_I \ddot{R}_I(t) &= -\frac{\partial}{\partial R_I} \langle \Psi_0 | H_e | \Psi_0 \rangle + \text{constraints} \\ \mu_i \ddot{\psi}_i(t) &= -\frac{\delta}{\delta \psi_i^*} \langle \Psi_0 | H_e | \Psi_0 \rangle + \text{constraints} \end{aligned} \tag{2}$$

For clarity, the explicit orthonormality constraints are excluded. The choice of an appropriate fictitious mass, μ_i, will ensure that there is adiabatic separation between the nuclear and the fictitious electronic degrees of freedom.[24,30] The simultaneous integration of the above equations of motion will ensure proper sampling of the electronic degrees of freedom and a faithful representation of the nuclear forces. Because one is no longer dependent on the convergence of the wave function to machine precision, a stable, energy-conserving MD simulation is obtained.[24,30] It should be pointed out that the choice of fictitious mass μ_i can have adverse affects on the trajectory if not properly monitored.[31−34] The protocol for choosing μ_i and its effect on observables has been known for a decade[33] and recently revisited.[31,32,34]

Although bulk condensed phase simulation using first-principles MD simulation is a mature field, the use of the aforementioned methodology can be challenging when applied to interfacial systems. In general, one needs larger system sizes to model interfacial systems. In sections 2.1 and 2.2, we will review two efficient implementations of the electronic structure problem that allow one to perform large-scale studies of interfaces. The first is the standard plane-wave formulation of density functional theory as it is implemented in the CPMD package.[35,36] The other is a hybrid method that takes advantages of both the plane-wave and real-space approaches to density functional theory.[37,38] Although there are other real-space methods present in the literature,[39−44] at present only the methods reviewed in sections 2.1 and 2.2 have been directly used for large applications relevant to aqueous systems and atmospheric science. For this reason, the scaling behavior of the plane-wave and Gaussian and plane-wave (GPW) hybrid scheme is discussed in detail and compared (see section 5) in such a way that the reader can make practical choices regarding system size and simulation protocol given the available computational resources. Furthermore, all methods presented here are well tested and have source codes that are freely available on the Internet.[36,38] It is hoped that this review will inspire more results and benchmarks of other first-principles methods as applied to the computationally demanding systems that are discussed in this review. Finally, in section 2.3, we will review the state-of-the-art methods in applying the proper boundary conditions necessary to treat interfacial systems.

2.1. Plane-Wave Approach

The KS-DFT as implemented within the framework of CP-MD (and the software package CPMD[35,36]) uses a plane-wave basis set to describe both the wave function and density. In the simplest form, the Kohn−Sham energy functional can be written as

$$E_{\text{KS}} = E_{\text{kin}}[\psi_i] + E_{\text{ES}}[n(\mathbf{r})] + E_{\text{XC}}[n(\mathbf{r})] \tag{3}$$

Here,

$$\begin{aligned} E_{\text{kin}} &= -\frac{1}{2}\int \mathrm{d}\mathbf{r}\ \psi_i \nabla^2 \psi_i \\ E_{\text{ES}} &= E_{\text{H}} - \sum_I \int \mathrm{d}\mathbf{r}\ V_{\text{core}}^I(\mathbf{r}) n(\mathbf{r}) + \sum_{I \neq J} \frac{Z_I Z_J}{\mathbf{R}_I - \mathbf{R}_J} \\ E_{\text{H}} &= \int \mathrm{d}\mathbf{r}\ \mathrm{d}\mathbf{r}'\ \frac{n(\mathbf{r}') n(\mathbf{r})}{\mathbf{r} - \mathbf{r}'} \\ n(\mathbf{r}) &= \sum_i |\psi_i|^2 \end{aligned} \tag{4}$$

where, n is the electronic density, Z is the nuclear charge, $\mathbf{R}_I$ denotes the Ith nuclear coordinate, and V_{core}^I is the potential due to the core electrons.[30] In practice, V_{core}^I is treated within the pseudopotential (PP) approximation.[45−47] Last, the functional form of the exact exchange−correlation (XC) operator, E_{XC}, is unknown. The first type of ap-

proximation used to compute the XC energy is based the local density approximation (LDA),

$$E_{XC}^{LDA}[n(\mathbf{r})] = \int \epsilon_{XC}^{LDA}(n(\mathbf{r}))n(\mathbf{r})\, d\mathbf{r} \quad (5)$$

Here, $\epsilon_{XC}(n(\mathbf{r}))$ is the XC energy per particle interacting with a uniform electron gas.[27] Although XC using LDA has been shown to give useful results for some chemical applications, a more commonly used approximation to compute the XC is called the generalized gradient approximation (GGA) where

$$E_{XC}^{GGA}[n(\mathbf{r})] = \int \epsilon_{XC}^{GGA}(n(\mathbf{r}),\nabla n(\mathbf{r}))\, d\mathbf{r} \quad (6)$$

In this formulation, the ϵ_{XC}^{GGA} is now dependent on both the density and the gradient of the density, giving a hint of nonlocal character.[27] Some popular GGA functionals that may be referred to in this review are BLYP,[48,49] PBE,[50] HCTCH,[51] TPSS,[52] and OLYP.[53] In addition, there are now hybrid XC functionals such as B3LYP,[54] PBE0,[55] and X3LYP,[56] which contains the exact exchange term present in HF.[57]

Although a variety of basis sets can be used within the CP-MD approach, the systems of interest to early users and developers of CP-MD method were those of periodic condensed-phase systems. Thus, the use of the translationally invariant plane-wave expansion is ideal with no basis set superposition error (BSSE) introduced. The plane-wave expansion for the single-particle orbitals takes on the form

$$\psi_i(\mathbf{r}) = \frac{1}{\sqrt{V}}\sum_{\mathbf{G}} c_{\mathbf{G}}{}^{i} \exp[i\mathbf{G}\cdot\mathbf{r}] \quad (7)$$

where V is the volume of the periodic supercell, $c_{\mathbf{G}}$ is the reciprocal-space coefficient to be optimized, and $\mathbf{G}$ is the reciprocal lattice vector. Thus, the electronic density, $n(\mathbf{r})$ becomes

$$n(\mathbf{r}) = \frac{1}{\sqrt{V}}\sum_{\mathbf{G}} n(\mathbf{G}) \exp[i\mathbf{G}\cdot\mathbf{r}]$$

$$n(\mathbf{G}) = \sum_i \sum_{\mathbf{G}'} c^i_{\mathbf{G}'-\mathbf{G}} * c^i_{\mathbf{G}'} \quad (8)$$

Here the "$*$" denotes complex conjugation. Given the definition of the orbitals and the density in the plane-wave basis, we are now able to discuss the efficiency of the computational strategy in computing E_{KS}.

To obtain the ground-state orbitals and density, we solve the self-consistent field (SCF) problem by zeroing the variations of E_{KS} with respect to the set of single-particle orbitals, ψ_i, namely,

$$\frac{\delta E_{KS}}{\delta \psi_i^*} = H_{KS}\psi_i \quad (9)$$

where the connection to eq 1 is established with $H_e = H_{KS}$. Here, H_{KS} is given by

$$H_{KS} = -\frac{1}{2}\nabla^2 + V_{KS}(\mathbf{r})$$

$$V_{KS}(\mathbf{r}) = V_H + V_{XC}$$

$$V_H = \int d\mathbf{r}' \frac{n_{tot}(\mathbf{r}')}{\mathbf{r}-\mathbf{r}'};\quad n_{tot}(\mathbf{r}) = n(\mathbf{r}) + n_{core}(\mathbf{r})$$

$$V_{XC} = \frac{\delta E_{XC}}{\delta n(\mathbf{r})} \quad (10)$$

where we assume that the external potential is only due to the bare nuclear charges. There are three main components of a plane-wave calculation: the computation of n and V_{KS} and the application of V_{KS} to the single-particle orbitals, ψ_i. In practice, the calculation of the total energy is done in real space, namely,

$$E_{KS} = \int d\mathbf{r}\, V_{KS}(\mathbf{r})n(\mathbf{r}) \quad (11)$$

The computation of the density from the orbitals in reciprocal space ($c^i_{\mathbf{G}}$) require N_{states} fast-Fourier transforms (FFT). Each FFT scales as $O(N_{grid} \log N_{grid})$, where N_{grid} denotes the number of real-space grid points.[58] The calculation of V_{KS} in real space requires the calculation of $V_{XC}(\mathbf{r})$ and $V_H(\mathbf{r})$. $V_{XC}(\mathbf{r})$ is constructed directly in real space, whereas $V_H(\mathbf{r})$ is computed via the reciprocal-space density, $n(\mathbf{G})/\mathbf{G}^2 = V_H(\mathbf{G})$ followed by a single FFT. The application of $V_{KS}(\mathbf{r})$ on ψ_i requires two FFTs for each state. The first transforms $c^i_{\mathbf{G}}$ to ψ_i, followed by the application of $V_{KS}(\mathbf{r})$ and transformation back to the new $c^i_{\mathbf{G}}$ where the calculation is repeated until self-consistency is achieved.

It should be clear from the above analysis that although the CPMD package is quite efficient, the algorithm necessary to perform an optimization of the wave function does not scale linearly with the number of states or real-space grid points (i.e., volume) and could be problematic for systems containing large amounts of free volume (see Figure 1). As we will find in sections 4 and 5, it is still possible to simulate physically relevant interfacial models with varying degrees of computational resources.

2.2. Hybrid Methods

As alluded to in section 2.1, the use of a plane-wave basis set in conjunction with FFT has made CP-MD simulations of systems ($N_{atom} < 100$) routine on modest computational resources. Unfortunately, systems of interest in this review, such as the simulation of an interface, or even a simple peptide requires much larger system sizes ($N_{atom} > 1000$), and applications of a plane-wave-based CP-MD method become impractical without state-of-the-art capability computing resources (see http://www.top500.org).

In light of this, the new hybrid methods based on using a mixed basis such as the Gaussian and plane-wave (GPW) and the Gaussian and augmented plane-wave (GAPW) approaches are emerging and look to be very promising.[32,37,59−61] The aforementioned methods comprise the QUICKSTEP module in the software suite CP2K.[38] In these hybrid approaches, atom-centered Gaussian-type orbitals (GTO) are used to describe the orbitals, while plane waves (PW) are used as an auxiliary basis set to describe the electronic density. Within the context of the GPW method, the PW expansion and its electronic density representation (denoted $n^{PW}(\mathbf{r})$ in this section) is similar to those discussed

in section 2.1. The electronic density, as described by GTO, can be written as

$$n^{\mathrm{GTO}}(\mathbf{r}) = \sum_{\mu\nu} P^{\mu\nu}\varphi_\mu(\mathbf{r})\varphi_\nu(\mathbf{r}) \tag{12}$$

where $\psi_i(\mathbf{r}) = \sum_\mu c_{\mu i}\varphi_\mu(\mathbf{r})$ are the single-particle orbitals expanded using primitive Gaussian, $\varphi_\mu(\mathbf{r})$, variational coefficients, $c_{\mu i}$, and the density matrix, $P^{\mu\nu} = \sum_i c_{\mu i}c^*_{\nu i}$. The flow of the GPW calculation is similar to that outlined in section 2.1, namely, the calculation of n and V_{KS} and the application of V_{KS} to the single-particle orbitals.[60] The differences lie in the details of the calculations. Because we have a real-space representation of the single-particle orbitals, $\varphi_\mu(\mathbf{r})$, the density can be constructed directly in real space by an efficient collocation of the primitive Gaussians.[60] Thus, the calculation of $n^{\mathrm{GTO}}(\mathbf{r})$ can be made strictly, $O(N_{\mathrm{states}})$. The calculation of the $V_{\mathrm{KS}}(\mathbf{r})$ is identical to that discussed in section 2.1. Because of the choice of plane waves for the auxiliary basis set, one can construct $n^{\mathrm{PW}}(\mathbf{r})$ with a single FFT from $n^{\mathrm{GTO}}(\mathbf{r})$, and one proceeds to $V_{\mathrm{H}}(\mathbf{r})$ in an identical fashion as that outlined in section 2.1. Thus, the use of a plane-wave auxiliary basis facilitates an N_{grid} log N_{grid} computation of E_{H} in eq 4 avoiding the unfavorable scaling of the multicenter integrals by a direct computation in real space using $\varphi_\mu(\mathbf{r})$. The construction of the XC potential in the GPW approach is identical to the plane-wave implementation in section 2.1. Finally, the KS matrix is calculated directly in real space using an efficient algorithm that takes advantage of a compact representation of $\varphi_\mu(\mathbf{r})$ and scales as $O(N_{\mathrm{states}})$.[60] The compact representation of $\varphi_\mu(\mathbf{r})$ previously alluded to also ensures that the KS matrix is sparse, and its diagonalization and subsequent application to $\varphi_\mu(\mathbf{r})$ can also be performed efficiently.[60] Thus, it is clear that the GPW method has the potential to perform calculations of large systems with remarkable efficiency. Having said that, there are some drawbacks to the method that should be briefly mentioned. First, the quality of a plane-wave calculation is controlled by a single variable, namely, the reciprocal-space cutoff for the plane-wave expansion, $\mathbf{G}_{\mathrm{cut}}$. The GPW calculation will depend on the quality of the basis (thus significant knowledge of traditional electronic structure calculations such as inclusion of split valence scheme or polarization function[57]), as well as the reciprocal-space cutoff for the plane-wave expansion of the density. Unfortunately, with the presence of atom-centered basis functions, we will introduce basis set superposition errors (BSSE).[57] The BSSE arises because of the dependence of the basis set on atomic positions. This gives arise to a nonuniform spatial variational flexibility that artificially lowers the energy. The effect of the BSSE on the condensed-phase environment has yet to be fully understood. The performance of the methods outlined in this section applied to systems relevant to this review will be discussed in section 5.

It should be noted that not all of the methods that are utilized in this review are based on the efficient solution of the KS-DFT. Periodic Hartree−Fock (HF) software is also available publicly and has been used to successfully treat interfacial systems using an automated geometry optimization but excludes the finite temperature MD.[62−65] The main difference between a periodic HF implementation and the GPW is twofold. First, the treatment of the electrostatics is usually performed in real space. Second, the XC functional is replaced with the HF exchange given by

$$E_{\mathrm{x}}^{\mathrm{HF}} = -\frac{1}{4}\sum_{ij}\int \frac{d\mathbf{r}\, d\mathbf{r}'}{|\mathbf{r}-\mathbf{r}'|}\psi_i^*(\mathbf{r})\psi_i(\mathbf{r}')\psi_j(\mathbf{r})\psi_j^*(\mathbf{r}')$$

Here i and j denote the state index and the "$*$" represents complex conjugation. The efficient implementation of the HF exchange has been outlined in the literature for both real- and reciprocal-space basis sets.[65−68]

Because the majority of this review deals with the KS-DFT solution to the electronic structure problem, it is only fair to discuss the limitations of some of the more popular density functionals in the plane-wave formulation as compared to standard basis set methods for the water dimer (a judicious choice for this review). The results are tabulated in Table 1, where the plane-wave results are taken from the current literature.[68] As one can see, with the exception of LDA and HF, all methods give comparable results. However, a more useful comparison would be to examine the performance of density functionals for the structure of water in the condensed phase.[68,69] Figure 2 shows the radial distribution function obtained by HF as compared to a well accepted empirical parametrization of liquid water (TIP4P).[246] It is clear from this result, as foreshadowed in Table 1, that pure HF is quite unsatisfactory when put to the test of finite temperature MD. Results in Figure 3 also show the performance of three exact exchange functionals, all of which give more satisfactory performance. Similar results have been obtained from a mixed quantum mechanics/molecular me-

Table 1. Structural Parameters (Distances in pm, Angles in deg) and Binding Energies (E_{b} in kcal/mol) for the Water Dimer by Todorova and Co-workers[68]

	plane-waves			6-311++G(3df,2p)		
functional	r(OO)	α(OHO)	E_{b}	r(OO)	α(OHO)	E_{b}[a]
LDA	272.9	168.1	8.61	271.3	168.3	8.85 (0.44)
BLYP	297.6	176.6	4.34	296.6	171.8	4.17
XLYP	293.0	171.6	4.57	295.3	173.5	4.42 (0.30)
PBE	293.7	177.2	4.56	288.9	172.0	4.92 (0.33)
TPSS	293.0	177.3	4.31	289.5	175.1	
B3LYP	294.1	174.8	4.63	293.2	174.1	4.53 (0.29)
X3LYP	293.3	171.9	4.96	290.8	171.7	4.97
HF	303.7	175.1	3.65	303.2	174.7	3.71 (0.22)
best first-principles	291.2	174.5	5.02			

[a] Binding energies for Gaussian basis set calculations are counterpoise corrected. The correction energy is given in parentheses.

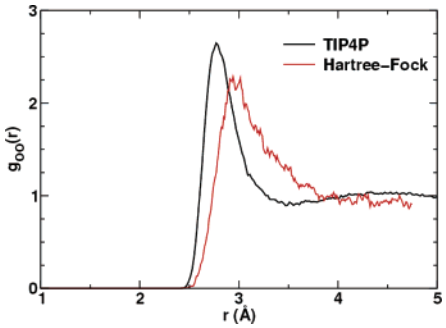

Figure 2. Comparison of oxygen−oxygen radial distribution functions between an empirically fitted water model (TIP4P[246]) and a KS-DFT based water using the B3LYP[49,54] exchange and correlation functional with a modified short ranged Hartree−Fock exchange term implemented within the plane-wave framework by Todorova et al.[68]

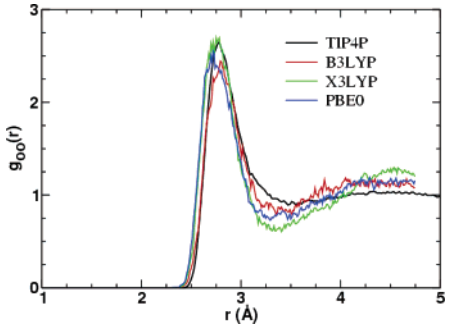

Figure 3. Comparison of oxygen−oxygen radial distribution functions adapted from the work of Todorova et al.[68] of TIP4P and three popular exchange and correlation functionals that include a modified short ranged Hartree−Fock exchange.

chanics (QM/MM) approach. In this study, the quantum mechanical region consisted of either one or two solvation shells of HF, B3LYP, and MP2 water. Both studies indicate that pure HF theory applied to the liquid phase does not yield a satisfactory structure.[68,69]

2.3. Boundary Conditions

One approach to simulating an interfacial system is to set up the system in slab geometry where the interface occupies the central portion of the supercell (see Figure 4). If one is

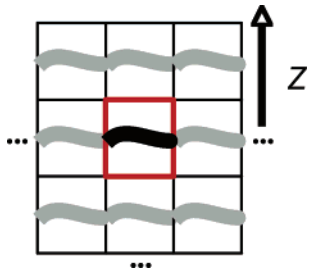

Figure 4. The central unreplicated supercell is depicted in red and contains the original interface with its two free surfaces, in black. Periodically replicated images of the interface are denoted in gray.

dealing only with short-range interaction potentials (i.e., Lennard-Jones potential), an elongation cell in the *z*-direction (perpendicular to the interface) such that the two free surfaces are outside the potential energy cutoff is sufficient to achieve a true 2D slab geometry. When one decides to employ long-range potentials, which are commonplace in the simulation of aqueous systems (i.e., electrostatic potentials), one has to approach the situation with caution. It's clear from Figure 4, in the presence of electrostatics, if the two free interfaces are not sufficiently far apart they could interact. Practically speaking, for MD simulations utilizing classical empirical potentials with point charges, the computational efficiency of the smooth particle-mesh ewald sum is efficient enough that one can include enough vacuum in the *z*-direction to again effectively reduce the problem to a 2D slab geometry[70] (see Figure 5). For first-principles approaches, in particular within the plane-wave formulation of KS-DFT, simply adding 100 Å of vacuum will render any problem computationally intractable. Because the plane-wave basis set gives an equal representation over the whole supercell regardless of the position of the nuclei (see section 2.1), the basis will fill the entire supercell increasing the number of plane waves as the volume, V (i.e., $O(V)$). In the hybrid approach discussed in section 2.2, basis functions are centered on

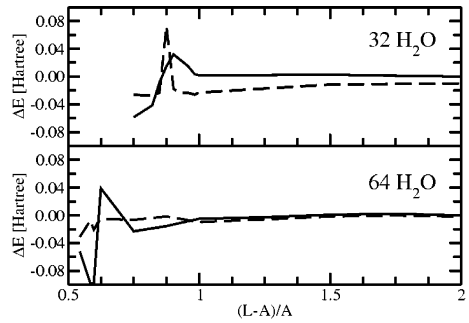

Figure 5. Energy convergence as a function of the supercell size in the *z* direction (L). The solid line represents the use of the 2D boundary condition, while the dashed line represents the use of the 3D boundary condition (A). Film thicknesses are 9.86 and 19.72 Å for 32 and 64 molecules, respectively. For the 2D boundary condition, convergence is guaranteed when $(L - A)/A = 1.0$, whereas when the 3D boundary condition is used, the amount of vacuum necessary to reach convergence depends on the system.

atoms, and thus there is no additional cost due to the increasing the number of basis functions. However, in the formulation outlined in section 2.2, one still computes the electronic density, $n^{PW}(\mathbf{r})$, in the plane-wave basis, which will scale linearly with the volume, $O(V)$. Whereas, in the plane-wave approach, the density is computed via N_{states} FFTs, all of which scale as $O(V)$, giving an overall $O(N_{states}V)$ scaling to compute the density in the presence of vacuum. The take-home message of this analysis is that in periodic formulations of KS-DFT using the hybrid method presented in section 2.2 or plane-wave approach, the cost of vacuum is $O(V)$ and $O(N_{states}V)$, respectively. Thus, to save on computational cost and, more importantly, to perform a sound simulation representing the slab geometry (see Figure 1), a 2D-implementation of the long-range interactions should be used.

Fortunately, there are many decoupling schemes that can be used, and all of them have roughly the same computational expense.[71−73] All are, in principle, exact and only differ in the details of the implementation. For this review, we will focus on the analytical decoupling schemes based on the original method of Martytna and Tuckerman, which we believe yields the most insight into the problem of decoupling periodic images.[30,71−73] Any formulation of computing the long-range interactions yields the following integral:

$$E_{LR} = \frac{1}{2}\int_V d\mathbf{r} \int_{\text{all space}} d\mathbf{r}'\, n(\mathbf{r})n(\mathbf{r}')\Phi(\mathbf{r}-\mathbf{r}') \quad (13)$$

where $\Phi(\mathbf{r} - \mathbf{r}')$ denotes the potential energy function.[72]

To illustrate the method, we will first compute the fully decoupled potential for the so-called cluster boundary conditions, that is, isolated system using an analytical approach.[73] For the case of an isolated cluster, the potential can be written

$$\Phi(\mathbf{r}) = \begin{cases} 1/r, & r > r_c \\ 0, & r \geq r_c \end{cases} \quad (14)$$

Here, r_c is given by $A < r_c < L - A$ as depicted in Figure 6. Using the common form of the reciprocal space density,

$$n(\mathbf{r}) = \frac{1}{V}\sum_{\mathbf{G}} \exp(i\mathbf{G}\cdot\mathbf{r})n(\mathbf{G}) \quad (15)$$

we obtain a final expression for the long range (LR) energy functional,

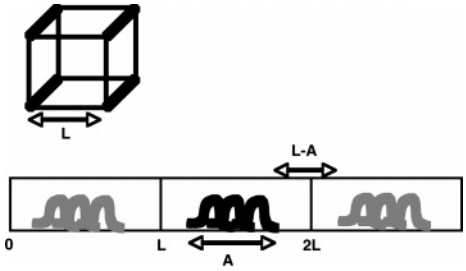

Figure 6. The isolated cluster (cube) and its periodic replication. The central charge density is represented in black, and the first two images to left and right are represented in gray. *L* and *A* are defined in Figure 5.

$$E_{\mathrm{LR}} = \frac{1}{2V^2}\int_V \mathrm{d}\mathbf{r} \sum_{\mathbf{G}} \exp(i\mathbf{G}\cdot\mathbf{r}) \int \mathrm{d}\mathbf{r}' \sum_{\mathbf{G}'} \exp(i\mathbf{G}'\cdot\mathbf{r}')\, \Phi(\mathbf{r}-\mathbf{r}')n(\mathbf{G})n(\mathbf{G}') \quad (16)$$

The screened potential for an isolated system (complete decoupling of all images) is given by

$$\Phi^{0\mathrm{D}}(\mathbf{G}) = \int_{r'<r_c} \mathrm{d}r' \exp(i\mathbf{G}\cdot\mathbf{r})\frac{1}{r'} = \frac{4\pi}{G^2}[1-\cos(Gr_c)] \quad (17)$$

This is distinct from the fully periodic 3D potential, which has the usual form of $4\pi/G^2$.

For the case of 2D, we will derive an appropriate screening potential to be added to the full 3D potential, $4\pi/G^2$. To proceed, we define the *z*-dimension of the central supercell to range from $z = -C/2$ to $C/2$. We then compute the electrostatic contribution from outside of the central supercell to obtain the screening function (see Figure 4). Thus, we are left with the following expression in analogy with eq 17:

$$\Phi^{2\mathrm{D}}_{\mathrm{screen}}(\mathbf{G}) = -\int_{\mathrm{slab}} \mathrm{d}\mathbf{r} \exp(i\mathbf{G}\cdot\mathbf{r})\frac{1}{\mathbf{r}} \quad (18)$$

Here "slab" denotes the region outside of the central supercell. We adopt cylindrical coordinates, *z*, *r*, and θ, where the reciprocal-space vector takes the following form: $\mathbf{G} = (g\cos\theta, g\sin\theta, g_z)$. Thus, we have

$$\begin{aligned}
\Phi^{2\mathrm{D}}_{\mathrm{screen}}(\mathbf{G}) &= -2\int_{C/2}^{\infty}\mathrm{d}z \exp(ig_z z)\int_0^{2\pi}\mathrm{d}\theta\int_0^{\infty} r\,\mathrm{d}r \exp(igr\cos\theta)\frac{1}{\sqrt{z^2+r^2}} \\
&= -2\int_{C/2}^{\infty}\mathrm{d}z\cos(g_z z)\int_0^{\infty}2\pi r\,\mathrm{d}r\, J_0(gr)\frac{1}{\sqrt{z^2+r^2}} \\
&= -4\pi\int_{C/2}^{\infty}\mathrm{d}z\cos(g_z z)\frac{1}{g}\exp(-gz) \\
&= \frac{-4\pi}{G^2}\exp(-gC/2)\left[\cos(g_z C/2) - \frac{g_z}{g}\sin(g_z C/2)\right] \quad (19)
\end{aligned}$$

Using the definition of the reciprocal vector in an orthorhombic box, namely, $g_z = n_z(2\pi/C)$, we obtain a final expression of the 2D screening function:[30,73]

$$\Phi^{2\mathrm{D}}_{\mathrm{screen}}(\mathbf{G}) = \frac{-4\pi}{G^2}(-1)^{n_z}\exp(-gC/2) \quad (20)$$

Similar formulations of 2D boundary conditions have been utilized with success,[74,75] and use of eq 20 to study aqueous liquid−vapor interfaces will be discussed in detail in section 5.

3. Spectroscopic Observables

Though the cost of using a first-principles interaction potential to study heterogeneous systems can be prohibitive, there is direct access to the spectroscopic observables and reactivity. In particular, the use of first-principles interaction potentials in periodic systems can make direct contact with infrared, Raman, and X-ray absorption experiments. In section 3.1, we will discuss the computation of infrared spectra from first-principles MD in the condensed phase, followed by the computation of Raman spectra using linear response theory in section 3.2. Last, we will give an overview of recent developments in the computation of X-ray absorption (XAS) in aqueous systems in section 3.3.

Since we are discussing interfacial systems, an experimental technique often used that takes advantage of the inherent anisotropy produced by the interface is the sum frequency generation (SFG) technique. The formal theoretical framework for the computation of SFG spectra is well developed.[76−79] However at present, the computational cost to compute SFG spectra within a first-principles MD simulation is not computationally feasible.

3.1. Infrared

Infrared (IR) spectroscopy is generally one of the most readily available spectroscopic tools. In the case of water, IR absorption reveals the underlying dynamics of water through its vibrations and bending, as well as intermolecular modes such as librations. As a result, the ability to theoretically compute the IR absorption of any simulated systems is ideal in helping the experimentalist interpret data with atomistic detail.

There is extensive literature on the computation of IR absorption using empirical force fields. Unfortunately, most of these methods suffer from uncertainty in the calculation of the electronic dipole, which is necessary to directly compute the intensity of the IR absorption. Unlike MD simulations utilizing classical empirical potentials, first-principles simulations should not suffer from this problem because the electric dipole moment is, in principle, available in any electronic structure calculation. The IR absorption coefficient, $\alpha(\omega)$, can be calculated as

$$\alpha(\omega) = \frac{4\pi\omega\tanh(\beta\hbar\omega/2)}{3\hbar n(\omega)cV}\int_{-\infty}^{\infty}\mathrm{d}t\, \mathrm{e}^{-i\omega t}\langle\mathbf{M}(t)\cdot\mathbf{M}(0)\rangle \quad (21)$$

where the use of classical nuclei is taken into account by the factor of $\tanh(\beta\hbar\omega/2)$, $n(\omega)$ is the refractive index, and $\mathbf{M}$ is the dipole moment.[80] Other more accurate forms for quantum corrections have been recently suggested.[81] The autocorrelation function for the total electronic contribution (ionic and electronic), $\langle\mathbf{M}(t)\cdot\mathbf{M}(0)\rangle$, can be computed directly from a first-principles simulation. One of the main problems with the computation of the electronic dipole moment is the inability to precisely define the position operator in a periodic system. A clever solution was found to this problem by

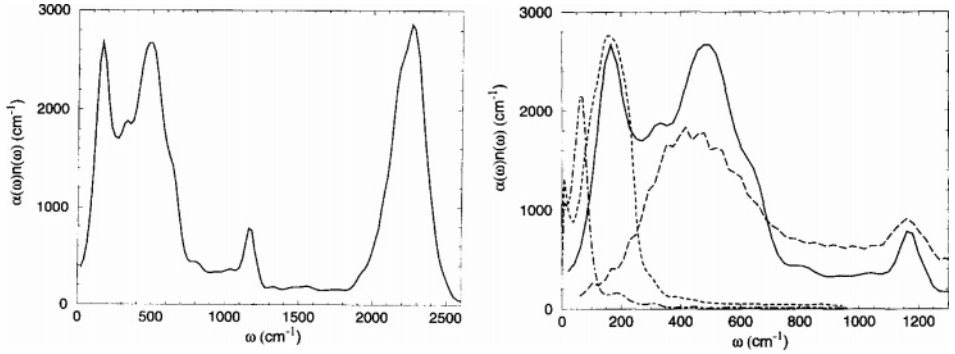

Figure 7. The computed IR absorption spectrum of D_2O. Solid line represents the computed IR spectrum, while dashed lines represent power spectra obtained from the correlation function of a specific nuclear degree of freedom only. Reprinted from *Chemical Physics Letters*, Vol. 277, Issue 5−6, P. Silvestrelli, M. Bernasconi, and M. Parrinello, Ab initio infrared spectrum of liquid water, page 478, Copyright 1997, with permission from Elsevier.

utilizing the so-called Berry's phase approach and computing the object,[82,83]

$$S_{mn} = \langle \psi_m | \exp(-G_\alpha r) | \psi_n \rangle$$
$$\varphi(G_\alpha) = \text{Im ln det } \mathbf{S} \qquad (22)$$

for reciprocal lattice vector G_α. In the Berry's phase picture, the electronic dipole moment is computed as

$$M_\alpha^{\text{el}} = \frac{2|e|}{|G_\alpha|}\varphi(G_\alpha) \qquad (23)$$

Further theoretical and technical details of this procedure can be found elsewhere.[80,82]

In Figure 7, a computed IR absorption spectrum utilizing KS-DFT for D_2O is shown where the electronic polarization was explicitly deduced from eq 23.[80] It was found that the method was able to reproduce the major features of the liquid D_2O spectrum when compared to experimental data, especially in the high-frequency regime. For the low-frequency regime associated with librational modes, it was found that a quantum correction scheme is necessary. This correction leads to identification of specific modes associated with antisymmetric hydrogen bonding stretching that would otherwise not have be possible to identify through the computation of a power spectrum.[80]

Although IR absorption is highly useful in elucidating dynamical behavior for both intramolecular and intermolecular interactions, the problem in using eq 23 to compute IR adsorption for the study of interfacial systems is that eq 23 is based on the total dipole moment and thus surface effects may be washed out. Fortunately, first-principles simulation also affords a local picture of the system dipole moment. A good approximation to the IR spectra is based on the computation of the charge centers of the molecule. Assuming that these charge centers carry the full electronic charge, and a known nuclear charge, we can compute the dipole moment for each individual molecule and use eq 21 with $\mathbf{M} = \sum_i \mathbf{M}_i^{\text{mol}}$, where $\mathbf{M}_i^{\text{mol}}$ is the dipole moment of the ith molecule. In practice, this partitioning of the charges is done through the maximally localized Wannier functions (WFs). The determination of the WFs is based on the Berry's phase approach outlined above. The WFs procedure can be boiled down to finding a unitary transformation that minimizes the spread, Ω_i, of each orbital[84−87]

$$\Omega_i = \langle \mathbf{r}_i^2 \rangle - \langle \mathbf{r}_i \rangle^2 \qquad (24)$$

where $\langle ... \rangle_i$ denotes the expectation value of the position operator with respect to the ith. The expectation value of the position of the WF, and hence its center, is given by

$$r_\alpha = \frac{2\pi}{L}\tilde{S}_{mn}$$
$$\tilde{S}_{mn} = \langle \psi_m U | \exp(-G_\alpha r) | U\psi_n \rangle \qquad (25)$$

where the U is the unitary transformation that minimizes the total spread, $\sum_i \Omega_i$ (we also assume that we are in a cubic simulation cell such that $G_\alpha = 2\pi/L$). The WF centers and functions are shown for a single water molecule in Figure 8.

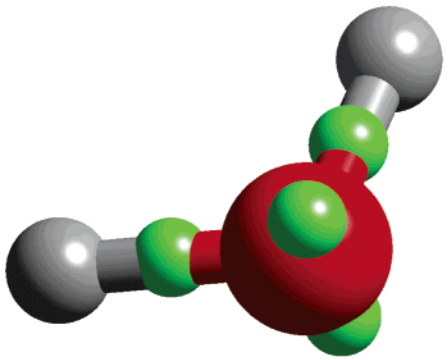

Figure 8. WF centroids (green spheres) of an isolated water molecule (oxygen is red; hydrogens are gray). Note that the two bond-centered centroids and lone-pair centroids form a tetrahedron and each carry charge $2e$.

3.2. Raman

Unfortunately, IR spectroscopy cannot always capture dynamical modes for all molecular systems. In particular, IR spectroscopy can only probe active modes where there is a change in molecular dipole. For Raman spectroscopy, the allowed transitions are those where the polarizability of a molecule changes, thus making IR and Raman spectroscopy complementary techniques. From first-principles MD simulation, it is possible to directly compute the Raman spectra within the Berry's phase scheme by computing the Fourier transform of the autocorrelation for the dynamic polarization tensor, $\tilde{\alpha}(t)$, within the variational density functional perturbation theory.[88] The polarizability tensor can be computed numerically as

$$\alpha_{\mu\nu}(t) = \frac{\partial^2 E}{\partial E_\mu \partial E_\nu} \tag{26}$$

throughout the simulation.[89] Quantum effects can also be incorporated if classical nuclei are used by multiplying by the factor $[1 - \exp(-\hbar\omega/(k_B T))/2]$.[90] But more specifically, the polarizability tensor can be separated into isotropic and anisotropic contributions, where the isotropic contribution to the Raman spectra is

$$I_{\mathrm{ISO}}(\omega) = \frac{N}{2\pi}\int_{-\infty}^{\infty} \mathrm{d}t\, \mathrm{e}^{-i\omega t} \langle \vec{\vec{\alpha}}(0)\cdot\vec{\vec{\alpha}}(t)\rangle \tag{27}$$

and the anisotropic piece is

$$I_{\mathrm{ANISO}}(\omega) = \frac{N}{2\pi}\int_{-\infty}^{\infty} \mathrm{d}t\, \mathrm{e}^{-i\omega t} \frac{1}{10}\langle \mathrm{Tr}[\vec{\vec{\beta}}(0)\cdot\vec{\vec{\beta}}(t)]\rangle \tag{28}$$

and the total intensity is $I(\omega) = I_{\mathrm{ISO}}(\omega) + {}^4/_3 I_{\mathrm{ANISO}}(\omega)$.[91] Like the simulated IR spectra, the calculation of Raman spectroscopy from first principles simulation is a powerful tool that can compliment experiments giving a particle-based picture to a specific spectroscopic signature.

The above methodology has been applied to the generation of a Raman spectrum for high-pressure ice. In Figure 9, the

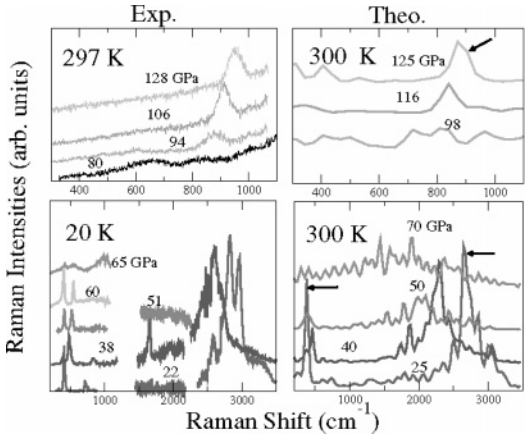

Figure 9. Experimental (left) and computed (right) Raman spectra for high-pressure ice.[89,92] Reprinted figure with permission from A. Putrino and M. Parrinello, *Physical Review Letters*, Vol. 88, No. 176401. Copyright 2002 by the American Physical Society.

general agreement between experiment and theory is remarkable.[89,92] The true advantage of being able to compute the Raman spectrum from a particle based method is the ability to look for individual contributions to the Raman spectrum and identify distinct intramolecular modes that would otherwise been difficult elucidate through experiments. Such is the case for high-pressure ice where it is predicted that ice X is symmetric and ice VII is a proton disordered system.[89] In the case of the ice−vapor interface (see section 4.1), such an analysis technique will be highly useful and relevant.

3.3. X-ray

Although X-ray absorption spectra (XAS) is a widely used technique in surface science, its utility in elucidating new insights into the structure of soft materials (including liquid−vapor and solid−vapor interfaces) is in its infancy. In particular, recent XAS experiments on water have challenged the conventional view of the structure of both bulk[93,94] and interfacial water.[95,96] Therefore, the ability to compute XAS from first-principles MD simulation will be of unique interest to experimentalist in helping to decipher spectra from XAS.

Unlike IR and Raman spectroscopy discussed in sections 3.1and 3.2 that can be computed utilizing classical models for the dipole and polarizability, XAS relies on some level of quantum theory to make contact with experimental spectra.[97] The oscillator strengths in XAS can be written as

$$I_{\mathrm{if}} = \frac{2}{3}\Delta E_{\mathrm{if}} |\langle \psi_{\mathrm{i}} | \mathbf{r} | \psi_{\mathrm{f}} \rangle|^2 \tag{29}$$

Here, the subscripts i and f denote initial and final states, respectively. The quantum chemical analysis that is necessary for the computation of the XAS spectra for aqueous systems has been employed in conjunction with configurations generated from MD utilizing classical empirical interaction potentials.[98] These calculations indicate that there is a large sensitivity of the computed XAS spectra to the distinct hydrogen-bonding configurations present in liquid water.[98]

However, this type of analysis is vulnerable to the differences in the classical force field from the quantum chemical model. Thus, a fully self-consistent first-principles treatment is preferable, if not imperative. It has recently been shown[99] that one can compute the XAS spectra of liquid water within the transition potential approach of DFT.[100,101] The XAS spectrum is obtained from analysis of a single wave function where the core level has half an electron removed ($1s^{1.5}2s^22p^4$). It is known that the use of a half-occupied core hole (HCH) takes care of relaxation effects up to second order.[102] Cavalleri et al. have implemented this scheme in CPMD within the PP approximation.[99] Although similar calculations have been performed within the CP-MD framework, differences in implementation have been focused around the reconstruction of the all-electron wave function from the pseudo-wave function of the final state for use in the transition probability and the use of fully occupied core hole (FCH) in the spectrum calculations.[103,104] The dipole selection rule for the specific case of aqueous systems implies that transitions from a 1s core level will be sensitive to the local p-character of the valence wave function.[99] Given this, Cavalleri et al. determined that for first-row elements (such as oxygen) the pseudo-p-character in the valence wave function is very close to the all-electron counterpart.[99] It was found that the difference in oscillator strengths for a variety of clusters using pseudo- and all-electron valence wave functions is negligible.[99] Moreover, a recent study by Cavalleri et al also examines the effects of the HCH and FCH protocols on the outcome of the spectra calculation.[105] Here it is argued that the use of a FCH can lead to results that are not consistent with experiment.[105]

In practice, the method employed by Cavalleri et al. does reproduce all the qualitative features of experimental XAS spectra for bulk ice (I*h*) and is in agreement with more established all-electron calculations.[99] Figure 10 depicts a typical spectrum for liquid water as obtained from Cavalleri et al.[99] using the plane-wave approach as discussed in section 2.1. The ability to compute XAS in condensed-phase environments will allow a better understanding of the very sensitive intermolecular interactions that play a vital role in the structure and chemistry at the surface.

4. Solid−Vapor Interfaces

As was alluded to in section 1, large-scale first-principles modeling is in its infancy with regards to finding solutions

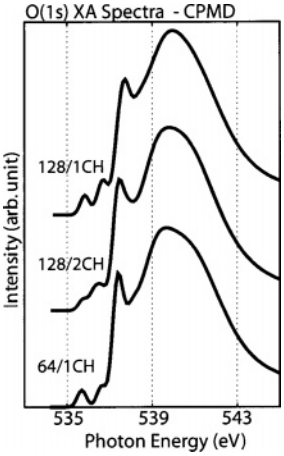

Figure 10. X-ray absorption spectrum of water generated using CPMD. This figure shows the agreement of the calculated spectra using 64 and 128 waters in a supercell. The bottom spectrum is obtained by generating a single core hole (CH), the top spectrum uses the same configuration as the 64-water supercell (only replicated) also generating a single CH, and the middle spectrum is generated utilizing the same 128 water configuration but also simultaneously generating the CH of the equivalent water molecule, thus indicating that finite size effects as well as interaction of neighboring CH do not significantly alter the spectra. Reprinted figure with permission from M. Cavalleri, M. Odelius, A. Nilsson, and L. G. M. Pettersson, *Journal of Chemical Physics*, Vol. 121, page 10065. Copyright 2004 by the American Institute of Physics.

to the myriad of fundamental questions in atmospheric science. However, given that first-principles calculations of heterogeneous systems require sizable computational resources, it has not stopped researchers from making significant progress toward understanding important atmospheric processes.[106−117] One instance where first-principles calculations have made significant progress toward understanding problems in atmospheric science is in the field of ozone depletion. In particular, the role of solid−vapor interfaces in the depletion of Artic and Antarctic ozone is of particular interest to the atmospheric community. The current conventional wisdom is that chlorinated compounds such as HCl and $ClONO_2$ are sequestered in polar stratospheric clouds (PSCs).[118−122] There are two predominant PSCs: the first (called type I) is thought to comprise nitric acid trihydrate (NAT); the second (type II) is ordinary ice.[118−122] Moreover, it has been experimentally verified that ice can act as a catalyst to reduce the barrier of reactivity to otherwise unreactive chlorinated gas-phase species (e.g., HCl, HOCl, and $ClONO_2$).[123] Thus, it is heterogeneous chemistry that will give rise to the production of the activated $Cl_2(g)$ via the proposed set of reactions.

$$ClONO_2(g) + H_2O(s) \xrightarrow{PSC} HOCl(g,ads) + HNO_3(ads) \quad (30)$$

$$HOCl(ads) + HCl(ads) \xrightarrow{PSC} Cl_2(g) + H_2O \quad (31)$$

$$ClONO_2(g) + HCl(ads) \xrightarrow{PSC} Cl_2(g) + HNO_3(s) \quad (32)$$

Equations 30 and 31 comprise a two-step mechanism, whereas eq 32 is a single step to form the active $Cl_2(g)$ product.[13,14] Upon examination of the aforementioned mechanisms, it becomes clear that the role of the interaction of HCl with the PSC provides a common denominator. Thus, there have been numerous experimental and theoretical studies designed to understand the uptake of HCl and its concomitant chemistry.[13,14,108−176] Measurements have characterized the uptake of HCl on well-characterized ice films (prototypical type II PSCs) with results ranging from 2×10^{13} to 4×10^{14} molecules/cm^2 under conditions approaching a PSC.[123,149−151] A variety of experiments indicate that ionic hydrates of HCl on ice films form at monolayer coverage (e.g., 1×10^{15} molecules/cm^2).[132,133,136,137,143,147,148,152,153] Conversely, experiments at submonolayer coverage suggest that molecular HCl is absorbed on the surface; however experiments are difficult to conduct and interpret within the conditions approaching a PSC, thus motivating the use of molecular simulation.[134,135,137,154−156] Attempts to understand and verify the above mechanisms have been addressed with large simulations based on classical empirical interaction potentials, reactive empirical interaction potentials, and first-principles interaction potentials in conjunction with smaller cluster models.[116,124−131,139−141,144,157−167] However, there is an emerging class of studies using first-principles interaction potentials of the more realistic semi-infinite surface based on methods outlined in sections 2.1 and 2.2.[106−114]

The idea of using a semi-infinite slab geometry to model the reactive interfaces is not done solely for the sake of vanity. It has long been known that surfaces of many solids can be disordered below the freezing point of the bulk liquid.[168] For example, there is speculation that the surfaces of type II PSCs may be disordered (quasi-liquid) and can lead to the enhancement of the uptake of HCl.[169] Naturally, this can only be modeled with a semi-infinite geometry depicted in Figure 1. The propensity, if not the existence, of the so-called quasi-liquid layer to aid in sequestering chlorinated compounds, as well as NO_x byproducts, is not understood.[4,111,112,114] Although experimentalists have produced a picture where surface ice is distinct from bulk, the temperature of this surface disordering effect is difficult to pin down due to its sensitivity to thermodynamic conditions (e.g., pressure) and impurities as well as the dependence on the different spectroscopic probes.[157,158,161,162,170−176] Thus, the use of first-principles simulation techniques may provide new insights into this difficult but important problem.

The role of type I PSCs in chlorine activation is currently less understood than that of type II. It is known from experiments that the efficiency of $Cl_2(g)$ production on NAT is strongly correlated with humidity and that production is at a greatly reduced rate than the corresponding rate on type II PSCs.[177] Thus for a specific set of conditions there can be "H_2O-rich" or "HNO_3-rich" NAT yielding very different catalytic behavior.[113,177] Experiments on the uptake of HCl on NAT have also been performed on surfaces resembling something between "H_2O-rich" and "HNO_3-rich" NAT yielding coverages similar to those measured on well-prepared ice surfaces.[123,151] However, experiments performed on the uptake of HCl on "HNO_3-rich" NAT indicate coverage about an order of magnitude less than those corresponding to the well prepared ice surfaces resembling type II PSCs.[177]

Thus, the goal of large-scale first-principles calculations reviewed here will be aimed at addressing the following issues regarding the structure and reactivity of PSCs: (i) The existence of the quasi-liquid layer (type II); (ii) The role of the quasi-liquid layer to yield the proposed catalytic activity (type II); (iii) prediction of the observed uptake and concomitant reactions of HCl on PSCs (type I and II); (iv) examination of possible heterogeneous reaction mechanisms leading to $Cl_2(g)$ (type I and II).

4.1. Ice

First-principles research regarding the nature of the clean ice−vapor interfaces has been conducted.[109,112] Static studies utilizing periodic HF were performed to examine the relative stability of different proton ordered phases of ice and examine surface relaxation.[109] This study also carefully examined the role of BSSE and showed that classical models may fall short in describing the proper energetics of unsatisfied hydrogen bonding (under-coordination) that is certainly present at interfaces.[109] Thus, the use of first-principles calculations to look at a finite temperature of ice−vapor interfaces is established. Both static and dynamic plane-wave calculations utilizing the CPMD code outlined in section 2.1 have been used to study the formation of the quasi-liquid layer on the clean ice−vapor interface.[111] In these studies, a supercell of hexagonal basal (0001) face of ice I*h*, which is thought to be the predominant surface under polar stratospheric conditions, is considered.[13,14] Figure 11 depicts the 32 water molecule supercell being made up of four bilayers. Again, as pointed out in section 2.3, there are two free surfaces, which must be kept from interacting by using either the appropriate 2D boundary conditions described in section 2.3 or an adequate amount of vacuum. Of course, vacuum comes at a price for the plane-wave approach (see section 2.3), and the delicate balance of amount of vacuum and computational efficiency must be considered. The aforementioned plane-wave calculations utilize vacuum ranging from 6 to 8 Å depending on the type of calculation being performed. In light of Figure 5, it is clear that at least 30 Å of vacuum is necessary to converge a 3D calculation of liquid water. It should be pointed out that the amount of vacuum needed to converge a 3D calculation will be dependent on configuration. Since the fluctuations of charge will give rise to different instantaneous multipole moments, it will in general take different amounts of vacuum to properly screen the two free interfaces. Thus, using 2*L* in the *z*-direction and 2D boundary conditions as discussed in section 2.3 is always the safest protocol. The Nose−Hoover thermostat was utilized for temperature control over the duration of the production runs.[178−180]

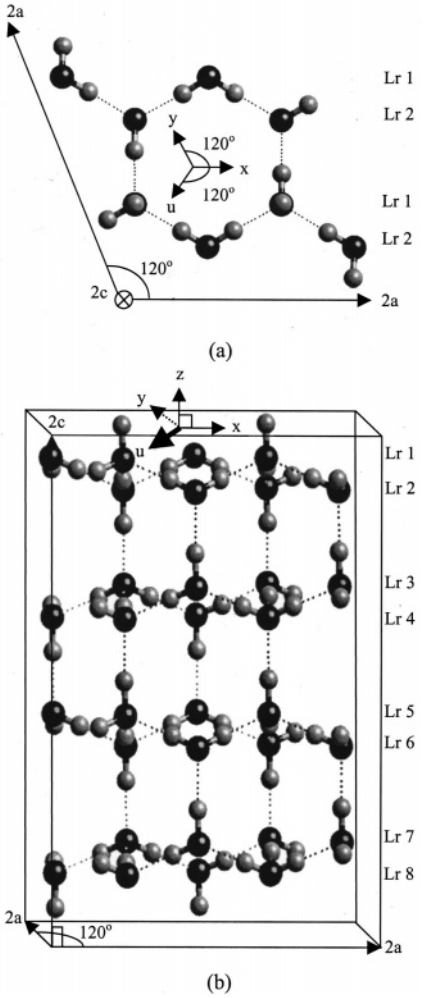

Figure 11. Supercell of hexagonal ice. The top panel represents the basal (0001) plane. The bottom panel is one of the six prism faces where the four bilayers are visible (i.e., bilayer one is made up of layers one and two). Dotted lines represent hydrogen bonds between oxygen (black) and hydrogen (grey). Reprinted figure with permission from Y. A. Mantz, F. M. Gieger, L. T. Molina, M. J. Molina, and B. L. Trout, *Journal of Chemical Physics*, Vol. 113, page 110733. Copyright 2000 by the American Institute of Physics.

To deduce the presence of a quasi-liquid layer, four first-principles simulations were performed over a temperature range of 190−310 K to investigate the effects of temperature on the formation of the quasi-liquid layer.[111] All four simulations were run for a duration of 1 ps with the fourth bilayer constrained not to move to better approximate a semi-infinite slab; thus effectively simulating one free interface.[111] One of the key findings was that the (0001) surface of ice is significantly disordered at 190 K. This is in contrast to the melting point for the 32 atom supercell of the ice surface, which was estimated to be at 220 K, which is below experiment.[111] This is in agreement with recent studies where the critical temperature of BLYP water was found to be lower by 15% and, invoking the law of corresponding states, also points to a lower melting point than experiment.[181,182]

Indicators of the onset of surface disordering yielding a quasi-liquid layer are borne out when one examines translational and rotational order parameters for the individual bilayers (see Figure 11). The order parameters used by Mantz et. al were identical to those proposed in a similar study utilizing classical empirical potentials.[183] The findings regarding the rotational and translational order parameters using first-principles interaction potentials were in good agreement with the classical empirical potentials given the caveat of trajectory length.[183] Translational disorder was also quantified in the *z* direction by computing average displacements from the fourth, fixed bilayer.[111] The results of this calculation corroborated experimental observations that layer one of bilayer one becomes disordered at 190 K whereas bilayers two and three remain ordered. A continuous transition to complete melting of the supercell was observed as the temperature was increased. Other indicators of the disordering are gleaned through examination of the radial distribution function (RDF) and mean square displacement (MSD) performed layer-by-layer.[111] With use of a reasonable guess for the normalization of the RDF for the layers, convincing evidence of a disordered first bilayer is obtained at 190 K with a first-peak height approaching that of a simulated bulk liquid of 32 water molecules.[111] The MSD at 230 K also seems to agree very well with a simulated bulk liquid indicating a melt. However, given the extremely short simulation time, these results are not definitive because the water molecule has not even diffused one molecular diameter in 1 ps. Having said that, the relative difference between the MSD of the different bilayers at 230 and 190 K clearly point to

the picture of a surface disordering at temperatures less than the bulk melting point. Last, a final simulation was performed to assess the effect of allowing bilayer four to remain free.[111] Properties that were affected were the heat capacity (presumably due to the additional degrees of freedom). The effects of fixing the fourth bilayer on the translation and rotational order parameter, as well as displacement in the *z* direction were inconclusive. In other words, the two free surfaces (bilayers one and four) did not behave identically.[111] However, this is most likely due to the extremely long simulation times that are required to equilibrate two free surfaces. This will be discussed in more detail in section 5.

Given the usual caveats of system size, choice of density functional, and trajectory length, there is certainly strong evidence put forth for the existence of a quasi-liquid layer using KS-DFT. The next step is to examine the role of microsolvation of chlorinated species (HCl, HOCl, and $ClONO_2$) leading to the proposed catalytic activity of the ice surface and the formation of activated $Cl_2(g)$ via eqs 30 and 31. For studies of mechanisms leading to the activated $Cl_2(g)$, both dynamic and static studies utilizing plane-wave and localized orbital schemes have been employed.

Calculations were performed on supercells of the hexagonal basal (0001) face of ice I*h* interacting with HCl.[106,107] Static studies utilizing localized orbitals within a periodic formulation of HF[62−64] were performed on a 1×2 supercell of ice (as opposed to the 2×2 supercell of Mantz et al.[111]) and focused on understanding the relative stabilities of molecular versus ionic HCl on the surface of ice.[106,107] After BSSE and correlation effects were taken into account, their findings indicated that it was energetically favorable to have molecular HCl inserted into an inclusion where a single surface water was displaced.[107] Furthermore, periodic substitution of HCl was favored more than the addition of a single HCl molecule leading to the conclusion that cooperative effects are indeed important.[107] Although the energetics of the substituted HCl molecule was not as favorable as that of neat ice surface (differing by 10−15 kcal/mol) it was found that the substitution of Cl^- and H^+ into the surface of ice differed by 3.1 kcal/mol.[107] Thus, these static calculations indicate that the dissociation of HCl to form ionic hydrates is most likely spontaneous[107] and can lead to surface sites with exposed chloride and can give rise to novel heterogeneous chemistry in line with experimental observations.[143,148] However, after chloride was inserted into subsurface layers, the resulting geometries were unstable leading to the conclusion that chloride will most likely remain on the surface at odds with the conclusions using empirical models.[13,14]

Static calculations utilizing both HF[106] and KS-DFT[114] were also performed to better understand the interaction of ice with HCl. In the KS-DFT study, particular attention was focused on the role of dangling bonds in promoting the dissociation of HCl.[114] Both 16[106,114] and 32[114] water molecules were used (2×1 and 2×2 supercell). In the KS-DFT study, surfaces with a different number of free (dangling) OH bonds were generated by considering all possible configurations where the hydrogen atoms satisfied the Bernal−Fowler ice rules.[114] Geometry optimizations were performed with the HCl molecule above the surface plane for five different slab conditions in the KS-DFT study (see Figure 12).[114] Under the same conditions that were utilized in the HF study (i.e., 16 molecule supercell, one HCl adsorbate, and two dangling OH bonds) results agreed to within 3 kJ/mol indicating that different levels of theory give consistent results.[114]

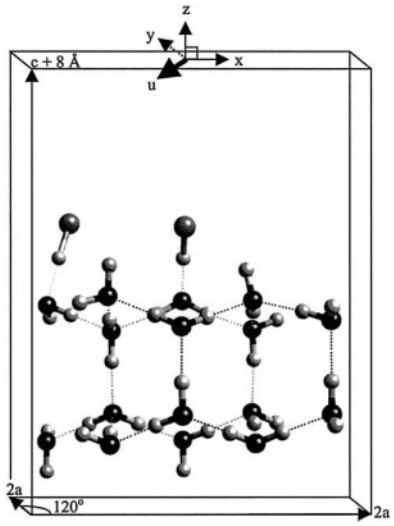

Figure 12. Side view of one of the six prism faces perpendicular to the (0001) basal plane of ice depicting the initial configurations of two HCl molecules, reproduced from ref 114. The supercell and vacuum region are superimposed. Color coding is the same as that in Figure 11, and Cl is represented by large gray spheres.

The results from the KS-DFT study suggest that the HCl adsorbed more favorably to sites where more free OH bonds are present in line with some experimental findings,[114,134,135] while other experiments suggest that surfaces with a high density of free OH bonds are representative of type II PSCs.[114,184] This could clearly be an indication of the microsolvation effects of a cluster of free OH groups stabilizing on the $Cl^{\delta-}$. Binding energies were also examined as a function of coverage.[114] For low coverage (1.4×10^{14} molecules/cm^2) the binding energies were slightly higher than for a coverage approaching that of a monolayer (2.8×10^{14} molecules/cm^2). Although the binding energies for low coverage were in agreement with cluster models resembling the surface geometry,[106,107,139,185] no dissociation was observed, although there was a lengthening of the H−Cl bond of 7%.

The dynamic effects of the adsorption of HCl on the hexagonal basal (0001) face of ice I*h* has also examined within a plane-wave formulation of KS-DFT.[112] Starting from an optimized configuration of a HCl above the (0001) face (see Figure 12), MD trajectories were performed at three different HCl adsorbing sites (1) to deduce the propensity for dissociation as a function of surface population of dangling OH bonds and (2) to examine the role of HCl on the disordering of the ice surface. From this study, it was found that spontaneous dissociation of HCl into H^+ and Cl^- is observed when an HCl molecule is interacting with a surface site containing two dangling OH bonds.[112] When geometry optimizations were performed at intermediate points of the trajectory, it was found that there is a 20 kJ/mol additional stabilization over the molecularly absorbed HCl.[106,114,116] Conversely, when HCl is absorbed over a site with only one free OH bond or placed further away from dangling OH bonds, no HCl dissociation was observed.[112] To understand these interactions, two simulations of a H_3O^+ and a Cl^- placed on a previously optimized ice slab were performed. One simulation yielded the stable formation of a contact ion pair, and the other yielded molecular HCl.[112] The binding energies of the contact ion pair and the molecular HCl compared well to the optimized structure of the HCl−ice system. This lead to the conclusion that dissociation of HCl is thermodynamically favorable under the appropriate conditions.[112]

Another question that can be addressed is the role of HCl on the formation of the quasi-liquid layer. Recall, that Gertner and Hynes, employing an empirical interaction potential, conjectured that dissociation of HCl was spontaneous and independent of the presence of a quasi-liquid layer,[13,14] which corroborates the results of the static localized orbital study.[107] Using the data generated with the dynamical study of HCl on ice, researchers examined the first peak of the oxygen−oxygen RDF to gauge the effects of surface disordering in the presence of associated and dissociated HCl. For the case of dissociated HCl at 150 K, the oxygen−oxygen RDF for bilayers one and two is similar to that obtained for the neat ice surface at 230 K.[112,113] In the presence of associated HCl, the oxygen−oxygen RDF is sharper than that of the theoretically predicted surface disordering temperature of the clean ice surface at 190 K. Thus, the results suggest that for high surface coverage of HCl in the presence of two dangling OH bonds, the disordering temperature is significantly depressed and extends into the second bilayer. It has been conjectured that in larger simulations of the ice with no quasi-liquid layer present, disordering may be a local phenomenon, putting this work in agreement with that of Gertner and Hynes.[13,14]

Finally, two detailed first-principles studies of the reactions given in eqs 30−32 were performed reaching very different conclusions.[108,110] The first study employed the plane-wave formation of KS-DFT using a 2 × 1 supercell where an additional layer in the *z* direction was added yielding a total of 24 water molecules.[110] Furthermore, it made use of the so-called ultrasoft pseudopotentials allowing for a significantly reduced basis set cutoff and thus dramatically reducing the computational expense.[45,186,187] It should be noted the structural and dynamical properties regarding liquid water using the ultrasoft pseudopotentials are still not understood.[188−190] This study also utilized a non-gradient-corrected functional. In light of the recent work of Todorova et al., this could be seen as problematic. [68] Nevertheless, the study did take place at finite temperature and concluded that reaction eq 31 can take place on the perfect hexagonal basal (0001) face of I*h* ice without surface disordering utilizing initial geometries of the HCl adsorbate similar to those in previous studies.[106,112,114] The reaction was initiated by the introduction of the HOCl gas molecule to the adsorbing HCl−PSC complex where the Cl−Cl distance was roughly 3 Å (see step a in Figure 13).[110] Because of the computational efficiency of the plane-wave formulation, potential of mean force calculations were performed utilizing the Cl−Cl distance as the reaction coordinate.[186,187] Each step of the free energy calculation was performed over roughly 1.5−2.5 ps of equilibration. The results of this study lead to a picture where the ice surface interacting with a physisorbed HCl becomes highly catalytic.[110] Furthermore, a picture emerges where the interacting HOCl molecule actually aids in the dissociation of the HCl molecule.[110] This view differs from the previously reviewed studies, which indicate that the HCl molecule can spontaneously dissociate on the ice surface.[107,112] The mechanism postulated from this plane-wave study suggests that upon dissociation of the HCl, the proton quickly migrates among two to three waters (see step b in Figure 13) leaving an isolated Cl^- to interact with a physisorbed HOCl molecule (see step c in Figure 13).[110] The formation of Cl_2(g) and water continues to proceed spontaneously (see step d in Figure 13). Liu et al. attribute the enhanced catalytic activity to the mobile proton, which facilitates the formation of water in the last step (see Figure 13).[110] The researchers also find that if one increases Cl−Cl distance in step b of Figure 13, the formation of molecular HCl through reverse proton migration is again achieved.[110]

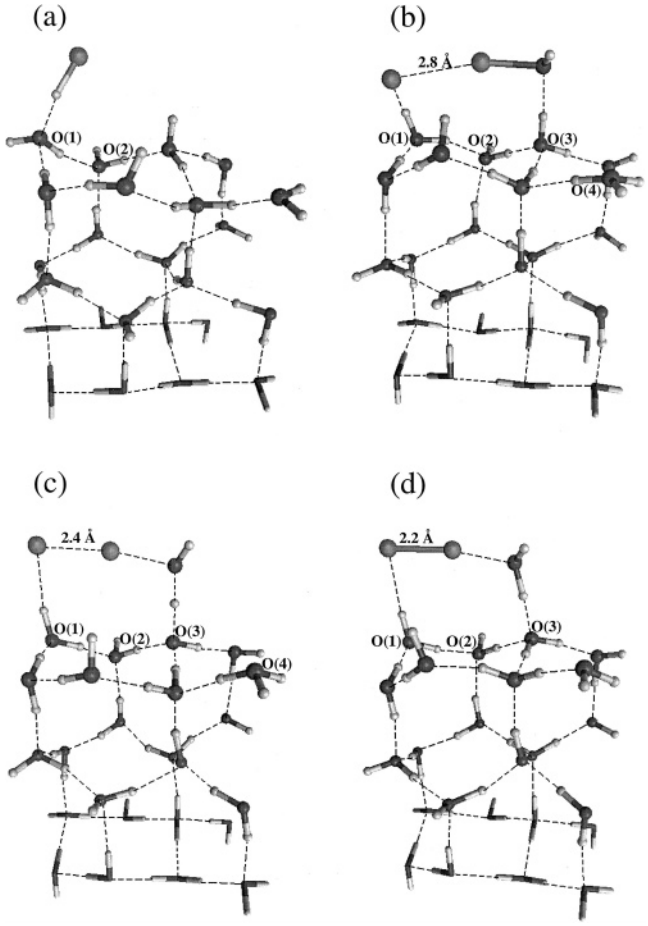

Figure 13. Details of the four-step reaction mechanism proposed in ref 110. Color coding is the same as that in Figure 12. Reprinted from *Chemical Physics Letters*, Vol. 309, Issue 5−6, Z. F. Liu, C. K. Siu, and J. S. Tse, Catalysis of the reaction HCl+HOCl → H_2O+Cl_2 on an ice surface, page 335, Copyright 1999, with permission from Elsevier.

In stark contrast to the aforementioned findings, a recent static first-principles study yields a more involved reaction mechanism when considering the reaction of eq 31.[108] Furthermore, this study makes reference to the previously mentioned dynamical study questioning the level of theory and the proton mobility, which gives rise to the enhanced catalytic activity.[108] The initial condition of this study does not assume the interaction of coadsorbed species of HCl and HOCl but rather the interaction of HOCl with an ice surface is already incorporated with Cl^- and H_3O^+ (see Figure 14) as described in earlier studies.[107] Thus, the sequence of reactions considered here given (in the notation of ref 108)

$$\mathrm{HCl} + \mathrm{ice} \rightarrow \mathrm{P_{hyCl}} \tag{33}$$

$$\mathrm{P_{hyCl}} + \mathrm{HOCl} \rightarrow \mathrm{Cl_2} + \mathrm{H_2O} + \mathrm{ice} \tag{34}$$

The top bilayer and the side view of the HCl hydrated surface, P_{hyCl}, are shown in Figure 14. More succinctly, these researchers considered the following hypothetical reaction mechanism: (1) activation of the surface through proton migration; (2) physisorption of HOCl with formation of a H^+−(OH)Cl−Cl^- complex; (3) concerted elongation of the

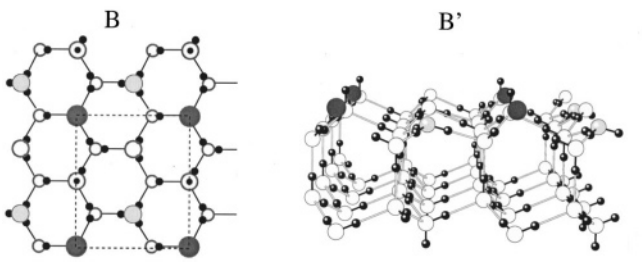

Figure 14. Top (B) and side views (B′) of the chlorinated P_{hyCl} surface. Oxygen is a small white circle, hydrogen is depicted by a small black filled circle, chloride is dark gray, and the hydronium oxygen is light gray. Reprinted figure with permission from S. Casassa, and C. Pisani, *Journal of Chemical Physics*, Vol. 106, page 9856. Copyright 2002 by the American Institute of Physics.

O−Cl bond and proton migration toward the molecule; (4) formation of $Cl_2(g)$ and H_2O.[108] The activatation of the P_{hyCl} species in step 1 occurs either via a two-step proton migration or via a proton rearrangement to produce a surface H_3O^+ moiety with a dangling OH.[108] Once the surface has been activated, the energetics of physisorption of the HOCl is compared in two scenarios where either the H or the Cl is in contact with the surface.[108] Comparing the energetics of both these possibilities suggests that direct interaction of the H of the physisorbed species with the activated P_{hyCl} is always more favorable. Last, actual reaction energetics were examined that produce the activated $Cl_2(g)$ and water. Reaction mechanisms were followed through two forms of the activated P_{hyCl}, namely, with proton movement (referred to as P^1_{hyCl} by Casassa et al.[108]) and with proton rearrangement (referred to as P^3_{hyCl} by Casassa et al.[108]). Both activated surfaces produced the same generic energy profile suggesting that reaction with these highly optimized ice surfaces is energetically costly yielding barriers on the order of 30−50 kcal/mol.[108]

Collecting the differences and similarities of the reviewed body of work pertaining to ice interfaces is illuminating. First, there is agreement with all of the studies that HCl will not spontaneously dissociate on a perfectly ordered surface of ice. The degree that disordering is necessary, either through the presence of a quasi-liquid layer or defects or even catalyzed through other physisorbed species, is still an open question. However, it should also noted that recent XAS experiments point to a picture where the presence of dangling bonds may not play a major role in the sequestering and the subsequent reaction of HCl.[152] All of the first-principles studies suffer from small system sizes and sampling protocols that are sure to have an affect on some of the conclusions that have been drawn. This is borne out most clearly in the reviewed work on the reaction mechanisms leading to the activated $Cl_2(g)$.[110] The plane-wave study was indeed ambitious by attempting to provide a free-energy surface along a prescribed reaction coordinate. However, the choice of this reaction coordinate (a simple distance between the two relevant chorine atoms) is most likely oversimplified and thus will only yield an upper bound to the free energy of the actual process. The fact that the reaction was actually barrierless is astonishing, and questions pertaining to the level of theory employed must be taken seriously. Conversely, the static HF study, although detailed, completely misses the relaxation of relevant degrees of freedom at a target temperature and cannot produce a true free energy. Thus, the seemingly insurmountable barrier of 30−50 kcal/mol is, again, an upper bound and most likely due to insufficient sampling of a reaction coordinate(s). In section 6, methodologies that allow one to deduce and probe probable reaction coordinates in complex systems will be reviewed.

It is also of interest to compare the use of different simulation protocols to the understanding of the initial stages of the reaction mechanisms put forth in eqs 30−32. As mentioned in section 4, there are substantial efforts being employed using clusters to determine the microsolvation of halide ions and acids.[163−167] As is pointed out by Bussolin et al.,[106] many of the quantum mechanical studies of clusters and halide ions are simply not relevant when compared directly to the question of adsorption of HCl on PSC. A notable exception is the work by Clary and co-workers who directly looked at the interaction of water with associated HCl in clusters (ranging from one to three water molecules). Here full geometry optimizations are performed, and although they do not find ionization to be be spontaneous, the stretching of the H−Cl bond is found to occur.[164] Clary and co-workers also performed a mixed QM/MM calculation treating two coordinates quantum mechanically (the H−Cl bond and distance of the HCl to the surface). Given the usual caveats of computing adsorption coefficients from extremely short trajectories and a simple reaction coordinate, it was found that the defects on an ice surface can have a profound effect on the adsorption of HCl on ice.[163,165,166] Although results using zero-temperature optimizations yield the associated acid as the stable state, it might be worth thinking about relative populations at relevant temperatures of the associated and dissociated states of the acid complex. A picture of the effects of microsolvation on acidity could be a useful concept to help further elucidate the early stages of the production of activated $Cl_2(g)$. This has been accomplished within the context of reactive empirical potentials.[13] Some useful algorithms that may bring us closer to this understanding utilizing first-principles methods will be discussed in section 6.

4.2. Nitric Acid Trihydrate

Recent first-principles studies have focused on bulk NAT,[191] as well as the less atmospherically relevant nitric acid monohydrate (NAM).[115] The appearance of first-principles calculations utilizing the KS-DFT method in conjunction with ultrasoft PPs on the NAM surface have also been performed presumably due to its smaller unit cell size (i.e., computationally more tractable).[117] This study was carried out on a 32 atom unit cell, which is far short of the 32 molecule supercell that has been used for the type II studies reviewed in section 4.1. Three calculations were performed where a HCl, a $ClONO_2$, and a H_2O molecule were randomly placed over the (100) surface of NAM.[117] It was found that all three molecules adsorbed parallel to the surface at distances ranging from 3.3 to 3.9 Å.[117] To test for catalytic activity, very short molecular dynamics simulations of 0.5 ps at 190 K were performed throughout which the three molecules were allowed to move from their geometry-optimized configurations on the surface. There was no appreciable differences in adsorbate geometries found leading to the conclusion that NAM is not a catalytic surface.[117] However, it is not clear that results gained from NAM surfaces will transfer over to NAT. Furthermore, large-scale studies of NAT surfaces are also hindered because there is no known classical empirical interaction potential to study bulk crystalline NAT, and no experimental consensus of the

structure of HCl on NAT surfaces has been determined.[113] Thus, it is absolutely necessary to use a first-principles interaction potential as a first step in the understanding of type I PSCs. To this end, a detailed static and dynamical study based on the plane-wave formulation of KS-DFT of the NAT−vapor interface and its interaction with HCl has been performed on a 112 atom $1 \times 1 \times 2$ supercell.[113]

To proceed, the determination of the thermodynamically favored low index faces needed to be selected. To this end, optimizations were carried out on six different low index facets, namely, the (100), ($\bar{1}$00), (010), (0$\bar{1}$0), (001), and (00$\bar{1}$). The surface energy of the (001) face was found to be the lowest, suggesting that this face will be the most relevant to conduct detailed studies of the atmospherically relevant reactions.[113] By testing 54 different initial conditions of HCl over the (001) interface of NAT, the relevant binding sites and geometries were determined.[113] It was found that 18 configurations produced a binding energy of at least 4 kJ/mol, but only one configuration produced a binding energy of 27 kJ/mol[113] typical for adsorption energies on type II PSCs.[106,112,114] This could be seen as an indication that "HNO_3-rich" NAT does not sequester as much HCl as type II PSCs in line with experimental results.[177] The site with the greatest affinity for HCl involves an interaction with a NO_3^- ion, and the possibility of interacting with at least one dangling OH bond of a nearby water.[113] Indeed, there are also two NO_3^- surface sites that would allow for the simultaneous interaction with two dangling OH bonds. When two trial configurations were optimized (HCl in the presence of one and two dangling OH bonds), it was found that even with the additional hydrogen bond formed with Cl^-, the two sites were nearly equal in energy[113] in contrast to studies on type II PSCs.[112,114]

To determine the fate of the adsorbed HCl (i.e., whether it remains associated or dissociates), molecular dynamics calculations were performed from the optimized configurations with one and two dangling OH groups interacting with HCl. The dynamics of the HCl interacting with two dangling OH groups produced a final configuration where the HCl was not interacting with either of the dangling OH bonds and was adsorbed perpendicular to the (001) interface.[113] Dynamical simulations from the geometry-optimized HCl interacting with a single dangling OH bond produced dissociation and subsequent reassociation of the HCl bond.[113] To further test the reliability of the dynamical results, configurations were generated based on the geometry-optimized interactions of HCl with one and two dangling OH bonds where HCl was dissociated. In all cases, after geometry optimizations were performed, it was found that the HCl remains associated at the (001) surface of NAT.[113]

5. Liquid–Vapor Interfaces

Aqueous liquid−vapor interfaces can also play a role in determining the chemistry that can occur in the troposphere. The relevant heterogeneous chemistry that can occur in the troposphere has been recently reviewed by Finlayson-Pitts.[192] Although the understanding of the bulk phases of hydrogen-bonding fluids is far from complete, the scientific impetus to understand these systems in more complex environments is far reaching. Furthermore, elucidating heterogeneous chemistry in the presence of an inorganic electrolyte and resolving the discrepancy in the mass accommodation coefficients for gases at the water−air interface is of paramount importance in atmospheric science.[1,193−195] This has, in part, led to a recent surge of pioneering scientific investigations within the chemical physics community to develop new surface-sensitive experimental techniques over the past 2 decades.[95,96,196−206] Recent experimental findings have revealed unexpected molecular structure and electronic distribution present at liquid−vapor interfaces.[95,96,196−206] In turn, these sophisticated techniques lead to a new challenge of connecting the results of these state-of-the-art experiments to the desired information on the microscopic properties of these liquid−vapor interfaces. Thus, the aforementioned experimental findings have stimulated a new realm of computational investigations whose central objective is to elucidate the structural, dynamic, and electronic properties of these important interfacial systems.

The first detailed MD calculations of the aqueous liquid−vapor interface were performed 15−20 years ago employing empirical pairwise additive potentials (Lennard-Jones and Coulomb interactions with fixed charges) as a model for liquid water.[207−209] These studies were the first quantitative calculations providing both structural and thermodynamic information about this important system. Although these MD studies pre-date the advent of surface-sensitive spectroscopies applied to the aqueous liquid−vapor interface, they have provided a template on which all subsequent MD studies were based, which has been covered in section 3.

Starting 10 years ago, pioneering spectroscopic investigations, using SFG technique, have provided an experimental picture of the detailed structure of the neat aqueous liquid−vapor interface.[198,200−203] These experiments pointed to structure at the interface being very distinct from the bulk. Two features in the spectra of these early experiments are noteworthy. First, a sharp peak at $\sim$3700 cm^{-1} indicates the presence of dangling hydrogen bonds at the interface. The second is a pronounced shoulder attached to the prominent peak at $\sim$3400 cm^{-1} present in bulk liquids that indicates the presence of a different hydrogen bonding arrangement at the surface. These SFG surface spectra of the neat liquid−vapor interface provided concrete data[198,200−203] that were amenable to a direct comparison with data obtained from MD simulations.[210,211] This MD study qualitatively elucidated the spectroscopic signals for both the existence of dangling OH bonds and the alternative hydrogen bonding arrangement at the surface.

Although it appears that classical empirical interaction potentials for water parametrized to reproduce bulk structural properties seem to perform well in the vicinity of the liquid−vapor interface, despite that the structural properties are adequately reproduced for water, the thermodynamic properties, such as surface tension and phase equilibria, indicate a deficiency in fixed-charge empirical models. Thus, a substantial amount of effort directed at developing water models that incorporate the polarization present at the aqueous liquid−vapor interface.[5,6,8] Moreover, additional experimental investigations on neat interfacial systems have led to further characterization of liquid−vapor interfaces and highlight the need for more accurate models.[95,96,196,197] As alluded to in section 3.3, XAS investigations have recently been carried out on both bulk and interfacial systems.[93−96,196,197] The results of these studies have challenged the conventional view of the structure of both bulk and interfacial water. The XAS results on bulk liquid water have produced a picture of a first solvation shell that remains controversial.[93,94] Studies of liquid microjets consisting of neat water or methanol produced strong evidence for different types of surface water

molecules at the liquid−vapor interfaces.[95,96,196,197] For the neat aqueous interface, an "acceptor-only" surface moiety is proposed wherein both hydrogen atoms of a surface water molecule extend out of the liquid[96] as opposed to the well recognized "single-donor" water for which only one hydrogen is dangling.[198−202,212] This finding is qualitatively different from earlier surface descriptions based on data obtained from SFG experiments. However, the sensitivity of this particular measurement to distinguish between acceptor-only and single-donor species may not be adequate.[198] The XAS measurements are sensitive to the precise nature of the solvating environment around a reference oxygen, whereas the SFG signal is sensitive to changes in vibrational frequencies produced by different hydrogen bonding environments.

Extended X-ray absorption fine structure (EXAFS) experiments were also used by Wilson et al.[95] to characterize liquid−vapor interfaces of water and methanol. The most intriguing finding for these neat systems is an outward surface relaxation (expansion) of ∼6% for the aqueous liquid−vapor interface whereas they find an inward relaxation (contraction) of ∼5% was observed for the neat methanol interface.[95,197] This outward relaxation for water could be related to charge rearrangement due to the unsatisfied bonding in the vicinity of the interface. To capture the fundamental physical chemistry revealed by the recent X-ray data,[93,95,96,196,197,206] the inclusion of many-body polarization effects in an unbiased manner through the use of first-principles interaction potentials is thus imperative.

A first attempt at using KS-DFT based methods to elucidate the aqueous liquid−vapor interface was performed using 32 water molecules.[213] Although this study provided interesting observations of surface moieties, the effects that small system size and boundary conditions can have on the outcome of this simulation need to be addressed. Figure 15

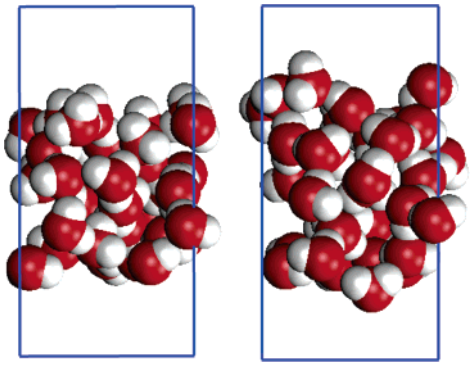

Figure 15. Side view (along *z*) of the initial (left) and final (right) configuration of a 32 water molecule aqueous liquid−vapor interface using full periodic boundary conditions with a supercell of $L \times L \times 2L$ (blue bounding box). After 5 ps of CP-MD, note the loss of a well-defined interface. All CP-MD simulation parameters are identical to those in ref 215. The supercell is superimposed in blue.

shows the initial and final configuration of 32 waters of a liquid−vapor interface using full 3D periodic boundary conditions. As one can see, after 5 ps of MD, the final configuration is not a stable liquid−vapor interface. The issue, whether boundary conditions or system size, can be addressed by performing the identical calculation with the 2D screening potential that was derived in section 2.3. The outcome of this simulation is depicted in Figure 16 and shows marked differences from Figure 15. In Figure 16, the interfaces are well defined and stabilized by the presence of the 2D-

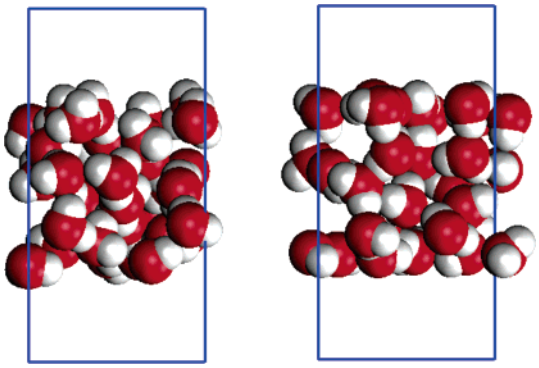

Figure 16. Side view (along *z*) of the initial (left) and final (right) configuration of a 32 water molecule aqueous liquid−vapor interface using a 2D screening function with $L \times L \times 2L$ (blue bounding box). After 5 ps of CP-MD, note the presence of a well-defined interface. All CP-MD simulation parameters are identical to those in ref 215.

screening function, but there is a clear layering effect, presumably due to the lack of a stable bulk region within the 32 water liquid−vapor interface. Recall that the simulations outlined in section 4 also contained on the order of 32 waters to describe the solid−vapor interfacial system. In these cases, one is able to constrain a layer to the bulk crystalline conditions to mimic interaction with a converged bulk material. Unfortunately, when liquid−vapor interfaces are simulated, no such protocol can be applied, and having a fully stabilized bulk region is imperative for a stable simulation. Thus, it is clear that *both* boundary conditions and system size will play a role in simulating a stable liquid−vapor interface.

Through the recent availability of tera-scale computing at Lawrence Livermore National Laboratory (LLNL) and the excellent scaling properties of CPMD,[30,35] a stable aqueous liquid−vapor interface with first-principles interaction potentials is now possible.[214,215] This calculation was performed on 216 water molecules at 300 K in a simulation cell of dimension 15 Å by 15 Å by 71.44 Å (see Figure 17). The decoupling of the periodic images was performed with methods outlined in section 2.3. The distance between the two free interfaces in the *z* direction was approximately 35 Å, indicating that there should be roughly 5−10 Å of bulk water. The initial configuration was obtained from classical molecular dynamics after an equilibration period of 100 ps at 300 K. After the initial wave function optimization, CPMD was performed for 7 ps. The simulation was performed on the 11 teraflop Multiprogrammatic Capability Resource (MCR) Linux cluster at LLNL (see http://www.top500.org) utilizing a total of 1440 CPUs.[30,35] The simulation parameters were chosen to ensure adiabaticity through out the MD simulation.[32,215] A Nosé−Hoover chain thermostat[178−180] was attached to every degree of freedom to ensure proper thermalization over the MD trajectory. This brute-force approach to thermostating was needed to ensure that a stable liquid−vapor interface was achieved. In principle, over a long enough trajectory, there will be a proper mixing of all the degrees of freedom to ensure that the entire interfacial system reaches the desired temperature. Because of the relatively short trajectories afforded by first-principles MD, without proper temperature control, there is the potential for the region in the vicinity of the interface to be significantly hotter than the corresponding bulk region.

The postprocessing of the electronic structure was performed with CP2K[38] (see section 2.2) by averaging 15 configurations over the last 4 ps using the QUICKSTEP[37,60]

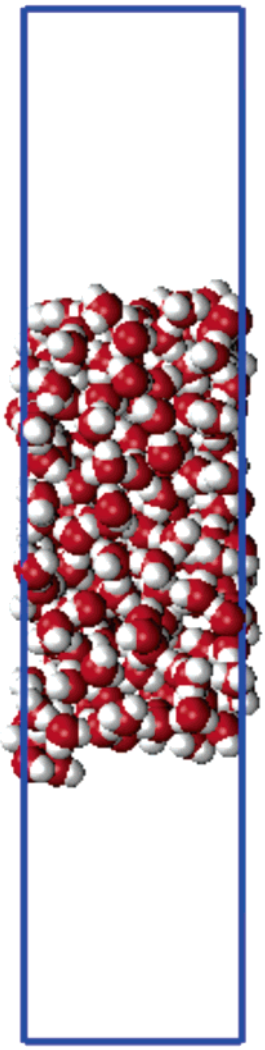

Figure 17. Side view (along *z*) of the supercell of the 216 water molecule aqueous liquid−vapor interface.[215] The supercell is superimposed in blue.

package in conjunction with the gradient-corrected BLYP functional,[48,49] dual-space psuedopotentails,[47] and a triple-ζ plus double polarization (TZV2P) basis set for the valence states.

Table 2 gives the extrapolated CPU years for a 10 ps trajectory using the methods discussed in sections 2.1 and 2.2. It is clear that the hybrid method discussed in section 2.2 performs very well for large interfacial systems.

Table 2. Extrapolated Total Number of CPU Years Required To Generate a 10 ps Trajectory Using a 0.097 fs Time Step with a Cutoff of 85 Ry and a 0.48 fs Time Step with a Density Cutoff of 280 Ry for CPMD and CP2K Benchmarks, Respectively[a]

	CPMD/CP2K	
no. of H_2O	bulk	interface
32	0.130/0.041	0.262/0.047
64	0.527/0.098	1.080/0.101
128	2.739/0.3527	6.392/0.5927

[a] The density for the bulk simulations was set at 1.0 g/mL, while for the simulated interfacial systems, the length of the supercell was set with $X = Y = Z/2$ to simulate the cost of a converged 2D periodic calculation (detailed discussion in section 2.3). The amount of CPU years was extrapolated from a benchmark performed over four CPUs for the 32 and 64 H_2O test systems and 16 CPUs for the 128 H_2O system where each CPU is an Intel Itanium2 running at 1.4 GHz. The simulation parameter can be found elsewhere.[32]

Before one can proceed with analyzing the liquid−vapor interface for novel hydrogen bonding moieties and reactivity, there must be some effort toward showing that one indeed has a stable interfacial system. This is most easily done with the computation of a density profile. Figure 18 depicts this

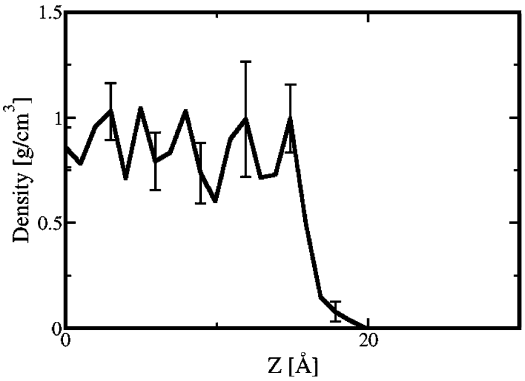

Figure 18. Density profile for the 216 molecule aqueous liquid−vapor interface.[215] Statistics were gathered over the last 4 ps of a 7 ps run, and $z = 0$ corresponds to the center of the interfacial slab.

profile, and it indeed suffers from lack of convergence. This is not due to a frozen interior region as can be gleaned from the examination of the orientational relaxation indicating that the librational peak for a hindered rotation is in good agreement with bulk studies.[215] The lack of smoothness can be explained by recalling that density profiles sample a discrete representation of space, and thus much longer trajectories are needed to obtain a smooth, converged density profile. We can also compute the volume of each individual water molecule as a function of its continuous spatial coordinate by utilizing Voronoi polyhedra.[216,217] This profile is depicted in Figure 19, along with the standard deviation

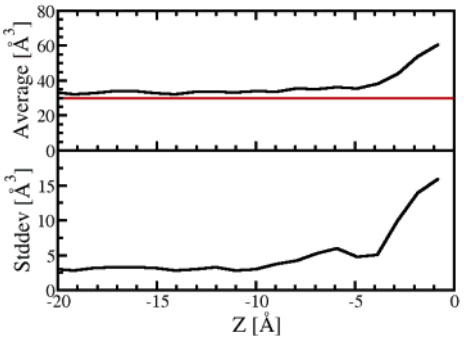

Figure 19. Plot of the Voronoi volumes (top) and their standard deviations (bottom) for the 216 molecule aqueous liquid−vapor interface.[215] The red horizontal line is at 29.9 Å^3/molecule indicating a density of 1 g/cm^3. Statistics were gathered over the last 4 ps of a 7 ps run, and $z = 0$ corresponds to the Gibb's dividing surface.

of the volumes as a function of the interfacial coordinate. It is clear that Figures 18 and 19 contain the same information. However, the salient feature of the Voronoi plot is that the signature of a stable bulk region is apparent when average volume/molecule as a function of the interfacial coordinate is examined. Figure 19 also corroborates the result obtained by examining the density profile in Figure 18, that the natural density of BLYP water may be less than 1 g/cm^3.[215] One also observes that the standard deviation of the Voronoi volumes in Figure 19 begins to increase well before the Gibbs' dividing surface defined here as the point where the

density becomes half of the bulk value. This is an indication that there may be surface relaxation in the vicinity of the liquid−vapor interface. Because even 7 ps (let alone the 1 ps trajectories reviewed in section 4.1) is not enough time to observe the identical average behavior of both free interfaces, all interfacial properties in this study are averaged over both free interfaces. To further corroborate the presence of surface relaxation, the average oxygen−oxygen distance in the bulk and interfacial regions can be computed using the minimum of the oxygen−oxygen RDF as a distance cutoff (see Figure 20). The interior region of the interface

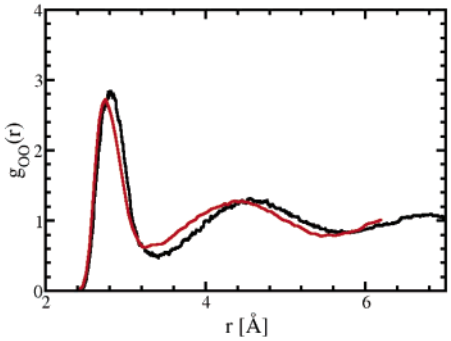

Figure 20. Oxygen−oxygen RDF (g_{OO}) of the interior of the 216 water aqueous liquid−vapor interface[215] (red) and a 64 water bulk simulation of liquid water simulated under the conditions in ref 32 (black).

has an average oxygen−oxygen distance of 2.93 Å in contrast to 2.96 Å in the vicinity of the interface. From this analysis, in addition to surface RDFs[215] that were computed, it is clear that there is a strong signature for a positive surface relaxation in agreement with recent experiments.[95]

The effect of the density of the interior of the interfacial slab being less than 1 g/cm^3 is manifest in the RDFs shown in Figure 20. It is clear that the first and second solvation shells are identical to a KS-DFT calculation of 64 waters at a fixed density of 1 g/cm^3, leading to a conclusion that 10% change in the density does not significantly distort the liquid structure.[215]

Given the usual caveats of system size and trajectory length, it is apparent that it is possible to stabilize an aqueous liquid−vapor interface with first-principles interaction potentials. It was alluded to earlier in this section that XAS experiments on interfacial water have detected the acceptor-only hydrogen bonding moiety. Given an MD trajectory, it is now possible to classify and count hydrogen bond populations at the interface. This procedure can be done using a reasonable definition of a hydrogen bond, and indeed, finite populations of both single-donor and acceptor-only moieties are present.[214,215] However, this should not come as a surprise; given that the configuration of the acceptor-only is not energetically forbidden, there will be some finite population. This is borne out in Table 3, where the acceptor-only populations are listed for a variety of classical empirical potentials and compared to the first-principles data using the hydrogen bond definition as suggested by Modig et al.[218] and used by Kuo and Mundy.[215] Clearly, the presence of a certain amount of acceptor-only hydrogen bond populations is not dependent on the underlying model to represent water. It is of interest to note that the surface IR spectrum can also be computed yielding the distinctive peak at 3700 cm^{-1}.[215] Although this surface IR verifies the existence of dangling OH bonds at the liquid−vapor interface, it cannot distinguish

Table 3. Comparison of the Acceptor-Only Populations of Various Water Models[a]

method	percentage of acceptor-only surface water molecules at 300 K
TIP4P[246]	12
TIP4P-fq[8]	13
TIP4P-pol[5]	7
BLYP[48,49]	19
expt	*b*

[a] Hydrogen bond parameters are identical to those found in ref 215. The classical empirical interaction potentials were simulated with Monte Carlo sampling utilizing 1600 atoms in a 30 Å × 30 Å × 100 Å supercell. [b] Not applicable.

between the acceptor-only and single-donor moieties. However, recent theoretical analysis of the SFG spectrum has found a spectroscopic signature for the so-called surface "wagging" mode, which is analogous to the acceptor-only species.[79]

A first-principles trajectory also offers a glimpse into the reactivity of this important system. An analysis needs to be performed that allows one to look at the frontier orbitals (i.e., the highest occupied molecular orbital (HOMO) and lowest unoccupied molecular orbital (LUMO)) of a particular molecule as a function of the slab coordinate. Although the KS states will give us the frontier picture that we desire, there is no way of associating a particular electronic state with a molecule and hence of defining its energy. In section 3.1, we describe a way of partitioning valence charge with the use of WFs.[219,220] Although WFs can be computed, they are not eigenfunctions of the H_{KS} and thus cannot be used for a frontier analysis. However, we can project H_{KS} into the WF basis,

$$H^{ij}_{WF} = \sum_k U^*_{ik} U_{jk} H^{ij}_{KS} \tag{35}$$

and rediagonalize subblocks of H_{WF} containing the states that belong to a particular molecule (see Figure 10) to obtain eigenvalues for each molecule. These eigenvalues are the so-called molecular states and can be used to construct HOMOs of individual molecules as a function of their chemical environment (in this case the distance from the Gibbs' dividing surface).

Using this methodology,[247] we can plot the HOMO and dipole moment (see section 3.1) of each water molecule in the aqueous liquid−vapor interface as a function of the interfacial coordinate. This is shown in Figure 21, and it indicates a trend toward higher reactivity and lower dipole

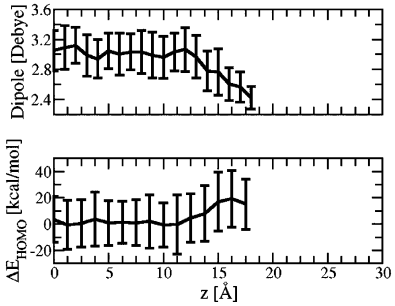

Figure 21. Dipole moment and molecular states of the 216 molecule aqueous liquid−vapor interface. Decrease in dipole moment as one approaches the interface was also found by Dang et. al using polarizable empirical interaction potentials.[6] Again, $z = 0$ denotes the center of the interfacial slab.

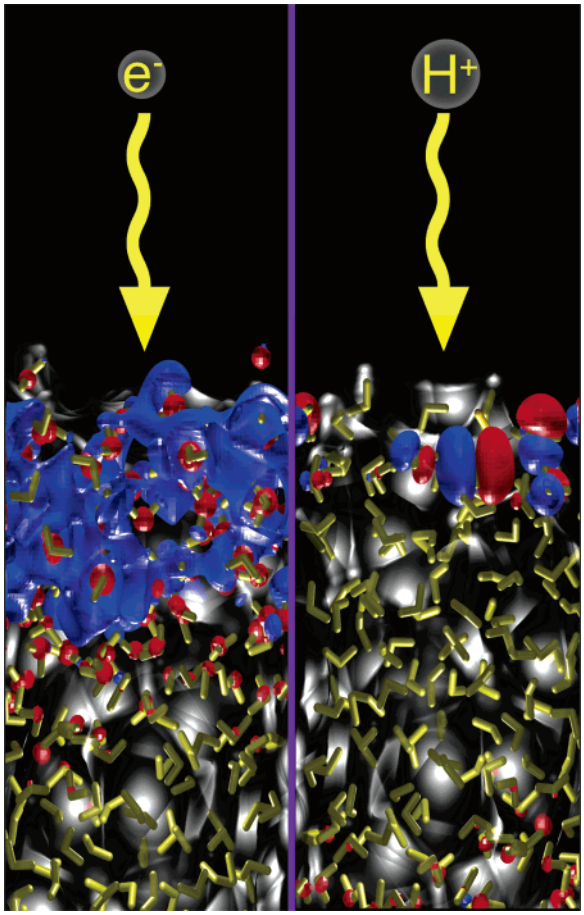

Figure 22. The KS HOMO (left) and LUMO (right) of the 216 water aqueous liquid−vapor interface.[215] The results indicate that the aqueous surface is reactive to both excess protons and electrons.

moment as one approaches the interfacial region. Last, Figure 22 depicts the HOMO and LUMO obtained via the KS states and shows for this particular snapshot that the interface is reactive to both excess protons and excess electrons, corroborating the molecular states analysis.

6. Conclusions and Future Directions

In summary, it is clear that the use of first-principles techniques for tackling the difficult problems associated with heterogeneous environments is an emerging area with immense potential. Atmospherically relevant interfaces (whether it be a PSC or an aerosol) pose many unanswered questions pertaining to reactivity that can be addressed with the use of the sophisticated models that have been reviewed here. It should now be clear to the reader that the methods for electronic structure calculations, outlined in section 2, are well suited for accurate and efficient studies of interfacial systems. Moreover, with the development and further use of hybrid methods to solve electronic structure problems, researchers will not have to rely on supercomputing hardware that is currently present at either supercomputing centers or national laboratories. Having fast electronic structure software suites that are publicly available should allow for rapid development of this important area of research.

One positive aspect that is true among all of the studies covered in this review is the careful examination of the theoretical findings in the framework of known experimental findings. Another common thread was the inability to pin down a precise reaction mechanism within a dynamical framework (with the exception of the mechanism for Cl_2 production put forth in section 4.1). This is in part because all of the first-principles-based studies did not aim to sample a reaction coordinate. Moreover, in the case of the liquid−vapor interfaces, further complications are introduced because of the relatively high diffusivity of the reactive species (such as ions), and one is not able to invoke symmetry to reduce the size of the system. One question that could be asked is whether the extremely short MD trajectories or zero-temperature electronic structure studies of semi-infinite systems are needed for deducing the mechanisms of atmospheric processes. In our opinion, the use of the semi-infinite system likely produces the correct interfacial structures that could be related to the observed enhanced reactivity (e.g., the presence of a quasi-liquid layer and the presence of more reactive states). However, the largest barrier to overcome to capture chemically relevant phenomena is the sampling of the complicated intermediate states, as well as the unbiased treatment of the interface that is postulated to undergo significant structural changes during a reaction. Both of these issues conspire in a way to make the sampling of these unknown reaction pathways extremely difficult, if not computationally prohibitive. Thus, in closing we will offer a review on treating rare events on a sound statistical mechanical basis that when combined with the first-principles methods outlined in section 2, could make the study of reaction mechanisms that take place in the vicinity of an interface tractable.

6.1. The Treatment of Rare Events

Understanding chemical reactions in complex environments (such as interfaces) will most certainly utilize a combination of smart sampling methods and fast electronic structure algorithms to gain insight into the free energetics that give rise to the observed phenomena. This is already borne out in a pioneering study of the heterogeneous oxidation of CO at the RuO_2 surface using the combination of DFT and kinetic Monte Carlo (kMC).[221] Here the so-called "first-principles kMC" extracts all the energetics of the elementary processes using first-principles methods and uses kMC to deduce the statistical mechanics. The result is the full characterization of an open system where gases come in contact with the surface, undergo a chemical reaction, and are then transported away. This method relies on the ability to enumerate important chemical reactions. Another feature of the first-principles kMC is that it does not require large computational resources. It should be noted that open systems can be treated entirely within the framework of a first-principles interaction potential in conjunction with the Gibbs' ensemble Monte Carlo to study phase equlibria.[181,182] However, these studies required enormous dedicated computer resources and thus make a reactive version of this algorithm a computational grand challenge. Even with the combination of first-principles interaction potentials and a kMC algorithm, one still must provide accurate chemical barriers, which presupposes some knowledge of the reaction coordinate to sample. However, it is clear from section 4 that the reaction mechanism for heterogeneous reactions is still unknown. Thus, the use of rare-event methods utilizing first-principles interaction potentials is well justified.

It is known that MD simulation on its own is very inefficient in sampling the free energy surface (FES), $V(\mathbf{r})$, due to the limited simulation time and high energy barriers.

Moreover, first-principles simulations suffer even more because the computational cost is even higher. This is very problematic since one of the main advantages of using first-principles interaction potentials over classical empirical potentials is the ability to look at bond formation. One common method for addressing the time-scale issue for sampling the FES with high energy barriers between local minima is through the use of umbrella sampling in conjunction with constrained MD.[222−224] In an umbrella sampling scheme, one first needs to identify a reasonable reaction coordinate to sample. Once the reaction coordinate is chosen, constrained MD is performed at regular intervals along the reaction coordinate yielding N independent simulations. The weighted population from the constrained MD simulation is then pieced together using a weighed histogram analysis method (WHAM).[222−224]

Through an umbrella sampling scheme in conjunction with WHAM, a FES can be constructed. However, there are drawbacks to using such a procedure. In particular, for a given system where a single one-dimensional reaction coordinate is known, N multiple independent simulations must be carried out using a biasing potential spaced out equally along the reaction coordinate. In the case where the reaction coordinate and FES must be described in two dimensions, N^2 independent simulations must be carried out.

To alleviate this unwanted scaling with the number of reaction coordinates, there have been many methods in the recent literature aimed at dynamically sampling rare events.[225−230] Most of these methods alter the dynamics to efficiently sample the configuration space.[226−230] However, to obtain the correct rates for the rare event of interest, transition path sampling is the method to be employed.[225] To effectively utilize the dynamical methods to sample rare events, one needs to characterize the initial and final states or have a detailed knowledge of the underlying potential governing the dynamics. Thus, to date, only a few of these methods have successfully been applied to systems with an arbitrary degree of complexity.[231−242]

One dynamical method that is having an impact on studying rare events in complex systems and thus deserves some additional attention is known as *Metadynamics.* Metadynamics is similar to the traditional umbrella sampling scheme outlined above with the exception that the biasing potential is not fixed but can self-adapt over the course of the simulation. Like an umbrella sampling scheme, a metadynamics simulation is carried out first by assuming that there are a finite number of relevant collective coordinates, $s_i(\mathbf{r})$, for any FES where $i = 1, n$. The only restriction on the choice of collective coordinates is that they must be derivable with respect to $\mathbf{r}$. It is common to express the collective variables as a distance, angle, or even coordination number with respect to a particular atom.[233−237,239,243−245] Once the relevant collective variables and coordinates are chosen, normal MD simulations are carried out where the evolution of the system evolves on the potential $V_{ext}(\mathbf{r},t)$ as described in section 2.1, where the potential is now time-dependent with the form

$$V_{ext}(\mathbf{r},t) = V_{FES}(\mathbf{r}) + V_{meta}(s,t) \tag{36}$$

where at $t = 0$, the time-dependent term $V_{meta}(s,t) = 0$. Once there is an adequate amount of sampling of the local FES, an additional potential is added to bias the trajectory away from the present landscape, namely,

$$V_{meta}(s,t) = \sum_t W \exp\left(-\frac{|\sigma - \sigma'|^2}{2\delta\sigma^2}\right) \tag{37}$$

Though this biasing potential can be of any form, Gaussians are chosen because of their ease of implementation and derivability with respect to the height and width (W and $\delta\sigma$, respectively), which are the parameters that determine the accuracy and efficiency of how one samples the FES. As the simulation proceeds, the aforementioned procedure is repeated and $V_{ext}(\mathbf{r},t)$ evolves according to $V_{meta}(s,t)$. Eventually the biasing potential, $V_{meta}(s,t)$, will converge to the negative of the actual FES.[243,244]

For more complex systems, metadynamics has also been shown to generate an equivalent FES when compared to umbrella sampling,[239] and the errors associated with a particular selection of W and $\delta\sigma$ are well characterized.[243,244] Furthermore, once a FES has been mapped out using a variety of different collective coordinates, an effective 1D parametrization can be constructed to take advantage of the accuracy of traditional umbrella sampling.[244] It should be pointed out that a true transition state can only be identified after the initial and final states are characterized and trajectories are harvested with the transition path sampling method.[225] Thus, transition path sampling, in conjunction with efficient dynamical schemes to find transition state candidates, are powerful and efficient methods that can be used with the methods outlined in this review to unravel the complex mechanisms that occur on atmospherically relevant aqueous interfaces.

7. Acknowledgments

We thank Larry Fried and Charlie Westbrook for their ongoing support of this work. We would like to thank J. Hutter for many discussions regarding CPMD. Conversations with Joost Vandevondele, Fawzi Mohamed, Matthew McGrath, and Matthias Krack regarding CP2K are gratefully acknowledged. Valuable discussions with Jens Mortensen regarding the analytical forms for the screening functions are also acknowledged. This work was performed under the auspices of the U.S. Department of Energy by the University of California Lawrence Livermore National Laboratory (LLNL) under Contract No. W-7405-Eng-48. Computer resources were provided by Livermore Computing.

8. References

(1) Knipping, E. M.; Lakin, M. J.; Foster, K. L.; Jungwirth, P.; Tobias, D. J.; Gerber, R. B.; Dabdub, D.; Finlayson-Pitts, B. J. *Science* **2000**, *288*, 301.
(2) Laskin, A.; Gaspar, D. J.; Wang, W. H.; Hunt, S. W.; Cowin, J. P.; Colson, S. D.; Finlayson-Pitts, B. J. *Science* **2003**, *301*, 340.
(3) Rowland, F. S. *Angew. Chem., Int. Ed.* **1996**, *35*, 1786.
(4) Molina, M. J. *Angew. Chem., Int. Ed.* **1996**, *35*, 1778.
(5) Chen, B.; Xing, J. H.; Siepmann, J. I. *J. Phys. Chem. B* **2000**, *104*, 2391.
(6) Dang, L. X.; Chang, T. M. *J. Chem. Phys.* **1997**, *106*, 8149.
(7) Dang, L. X.; Smith, D. E. *J. Chem. Phys.* **1993**, *99*, 6950.
(8) Rick, S. W.; Stuart, S. J.; Berne, B. J. *J. Chem. Phys.* **1994**, *101*, 6141.
(9) Warshel, A.; Weiss, R. M. *J. Am. Chem. Soc.* **1980**, *102*, 6218.
(10) Lobaugh, J.; Voth, G. A. *J. Chem. Phys.* **1996**, *104*, 2056.
(11) Sagnella, D. E.; Tuckerman, M. E. *J. Chem. Phys.* **1998**, *108*, 2073.
(12) Walbran, S.; Kornyshev, A. A. *J. Chem. Phys.* **2001**, *114*, 10039.
(13) Gertner, B. J.; Hynes, J. T. *Faraday Discuss.* **1998**, *110*, 301.
(14) Gertner, B. J.; Hynes, J. T. *Science* **1996**, *271*, 1563.
(15) Head-Gordon, M. *J. Phys. Chem.* **1996**, *100*, 13213.
(16) Burnham, C. J.; Li, J. C.; Xantheas, S. S.; Leslie, M. *J. Chem. Phys.* **1999**, *110*, 4566.

(17) Burnham, C. J.; Xantheas, S. S. *J. Chem. Phys.* **2002**, *116*, 5115.
(18) Burnham, C. J.; Xantheas, S. S. *J. Chem. Phys.* **2002**, *116*, 1479.
(19) Burnham, C. J.; Xantheas, S. S. *J. Chem. Phys.* **2002**, *116*, 1500.
(20) Xantheas, S. S.; Burnham, C. J.; Harrison, R. J. *J. Chem. Phys.* **2002**, *116*, 1493.
(21) Goldman, N.; Fellers, R. S.; Brown, M. G.; Braly, L. B.; Keoshian, C. J.; Leforestier, C.; Saykally, R. J. *J. Chem. Phys.* **2002**, *116*, 10148.
(22) Goldman, N.; Leforestier, C.; Saykally, R. J. *Philos. Trans. R. Soc. A* **2005**, *363*, 493.
(23) Goldman, N.; Saykally, R. J. *J. Chem. Phys.* **2004**, *120*, 4777.
(24) Car, R.; Parrinello, M. *Phys. Rev. Lett.* **1985**, *55*, 2471.
(25) Hohenberg, P.; Kohn, W. *Phys. Rev.* **1964**, *136*, B86.
(26) Kohn, W.; Sham, L. A. *Phys. Rev. A* **1965**, *140*, 1133.
(27) Parr, R. G.; Yang, W. *Density-functional theory of atoms and molecules*; Oxford University Press, Clarendon Press: New York, 1989.
(28) Kohn, W.; Becke, A. D.; Parr, R. G. *J. Phys. Chem.* **1996**, *100*, 12974.
(29) Pulay, P. *Mol. Phys.* **1969**, *17*, 197.
(30) Marx, D.; Hutter, J. In *Modern Methods and Algorithms of Quantum Chemistry*; Grotendorst, J., Ed.; John von Neumann Institute for Computing: Forschungszentrum Julich, 2000; Vol. 1.
(31) Grossman, J. C.; Schwegler, E.; Draeger, E. W.; Gygi, F.; Galli, G. *J. Chem. Phys.* **2004**, *120*, 300.
(32) Kuo, I. F. W.; Mundy, C. J.; McGrath, M. J.; Siepmann, J. I.; VandeVondele, J.; Sprik, M.; Hutter, J.; Chen, B.; Klein, M. L.; Mohamed, F.; Krack, M.; Parrinello, M. *J. Phys. Chem. B* **2004**, *108*, 12990.
(33) Pastore, G.; Smargiassi, E.; Buda, F. *Phys. Rev. A* **1991**, *44*, 6334.
(34) Schwegler, E.; Grossman, J. C.; Gygi, F.; Galli, G. *J. Chem. Phys.* **2004**, *121*, 5400.
(35) *CPMD*, 3.9 ed.; Copyright IBM Corp 1990−2001, Copyright MPI fur Festkorperforschung Stuttgart 1997−2005.
(36) CPMD. http://www.cpmd.org.
(37) Lippert, G.; Hutter, J.; Parrinello, M. *Mol. Phys.* **1997**, *92*, 477.
(38) CP2K. http://cp2k.berlios.de.
(39) Liu, Y.; Yarne, D. A.; Tuckerman, M. E. *Phys. Rev. B* **2003**, *68*, No. 125110.
(40) Fattebert, J. L.; Bernholc, J. *Phys. Rev. B* **2000**, *62*, 1713.
(41) Fattebert, J. L.; Gygi, F. *Comput. Phys. Commun.* **2004**, *162*, 24.
(42) Soler, J. M.; Artacho, E.; Gale, J. D.; Garcia, A.; Junquera, J.; Ordejon, P.; Sanchez-Portal, D. *J. Phys.: Condens. Matter* **2002**, *14*, 2745.
(43) Goedecker, S. *Rev. Mod. Phys.* **1999**, *71*, 1085.
(44) Varga, K.; Zhang, Z. Y.; Pantelides, S. T. *Phys. Rev. Lett.* **2004**, *93*, No. 176403.
(45) Vanderbilt, D. *Phys. Rev. B* **1990**, *41*, 7892.
(46) Troullier, N.; Martins, J. L. *Phys. Rev. B* **1991**, *43*, 1993.
(47) Goedecker, S.; Teter, M.; Hutter, J. *Phys. Rev. B* **1996**, *54*, 1703.
(48) Becke, A. D. *Phys. Rev. A* **1988**, *38*, 3098.
(49) Lee, C.; Yang, W.; Parr, R. G. *Phys. Rev. B* **1988**, *37*, 785.
(50) Perdew, J. P.; Burke, K.; Ernzerhof, M. *Phys. Rev. Lett.* **1996**, *77*, 3865.
(51) Hamprecht, F. A.; Cohen, A. J.; Tozer, D. J.; Handy, N. C. *J. Chem. Phys.* **1998**, *109*, 6264.
(52) Tao, J. M.; Perdew, J. P.; Staroverov, V. N.; Scuseria, G. E. *Phys. Rev. Lett.* **2003**, *91*, No. 146401.
(53) Handy, N. C.; Cohen, A. J. *J. Chem. Phys.* **2002**, *116*, 5411.
(54) Becke, A. D. *J. Chem. Phys.* **1993**, *98*, 5648.
(55) Adamo, C.; Barone, V. *J. Chem. Phys.* **1999**, *110*, 6158.
(56) Xu, X.; Goddard, W. A. *Proc. Natl. Acad. Sci. U.S.A.* **2004**, *101*, 2673.
(57) Jensen, F. *Introduction to Computational Chemistry*; Wiley: Chichester, U.K., New York, 1999.
(58) Press, W. H. *Numerical recipes in C: the art of scientific computing*, 2nd rev. ed.; Cambridge University Press: Cambridge, U.K., New York, 1997.
(59) Lippert, G.; Hutter, J.; Parrinello, M. *Theor. Chem. Acc.* **1999**, *103*, 124.
(60) VandeVondele, J.; Krack, M.; Mohamed, F.; Parrinello, M.; Chassaing, T.; Hutter, J. *Comput. Phys. Commun.* **2005**, *167*, 103.
(61) VandeVondele, J.; Mohamed, F.; Krack, M.; Hutter, J.; Sprik, M.; Parrinello, M. *J. Chem. Phys.* **2005**, *122*, 014515.
(62) Pisani, C.; Dovesi, R.; Roetti, C. *Hartree−Fock Ab Initio Treatment of Crystalline Systems*; Springer: Berlin, 1988.
(63) Pisani, C.; Cora, F.; Nada, R.; Orlando, R. *Comput. Phys. Commun.* **1994**, *82*, 139.
(64) Dovesi, R.; Saunders: V. R.; Roetti, C.; Causa, N.; Harrison, N. M.; Orlando, R.; Apra, E. *CRYSTAL95 User's Manual*; Universita di Torino: Torino, 1996.
(65) Dovesi, R.; Orlando, R.; Civalleri, B.; Roetti, C.; Saunders, V. R.; Zicovich-Wilson, C. M. *Z. Kristallogr.* **2005**, *220*, 571.
(66) Gygi, F.; Baldereschi, A. *Phys. Rev. B* **1986**, *34*, 4405.
(67) Chawla, S.; Voth, G. A. *J. Chem. Phys.* **1998**, *108*, 4697.
(68) Todorova, T.; Seitsonen, A. P.; Hutter, J.; Kuo, I. F. W.; Mundy, C. J. *J. Phys. Chem. B*, published online December 6, 2005, http://dx.doi.org/10.1021/jp055127v.
(69) Xenides, D.; Randolf, B. R.; Rode, B. M. *J. Chem. Phys.* **2005**, *122*, 174506.
(70) Darden, T.; York, D.; Pedersen, L. *J. Chem. Phys.* **1993**, *98*, 10089.
(71) Hockney, R. W. *Methods Comput. Phys.* **1970**, *9*, 136.
(72) Martyna, G. J.; Tuckerman, M. E. *J. Chem. Phys.* **1999**, *110*, 2810.
(73) Mortensen, J. J.; Parrinello, M. *J. Phys. Chem. B* **2000**, *104*, 2901.
(74) Minary, P.; Tuckerman, M. E.; Pihakari, K. A.; Martyna, G. J. *J. Chem. Phys.* **2002**, *116*, 5351.
(75) Barnett, R. N.; Landman, U. *Phys. Rev. B* **1993**, *48*, 2081.
(76) Morita, A.; Hynes, J. T. *Chem. Phys.* **2000**, *258*, 371.
(77) Morita, A.; Hynes, J. T. *J. Phys. Chem. B* **2002**, *106*, 673.
(78) Perry, A.; Ahlborn, H.; Space, B.; Moore, P. B. *J. Chem. Phys.* **2003**, *118*, 8411.
(79) Perry, A.; Niepert, C.; Ridley, C.; Space, B.; Moore, P. *Phys. Rev. E* **2005**, *71*, No. 050601(R).
(80) Silvestrelli, P. L.; Bernasconi, M.; Parrinello, M. *Chem. Phys. Lett.* **1997**, *277*, 478.
(81) Iftimie, R.; Tuckerman, M. E. *J. Chem. Phys.* **2005**, *122*, 214508.
(82) Kingsmith, R. D.; Vanderbilt, D. *Phys. Rev. B* **1993**, *47*, 1651.
(83) Marzari, N.; Vanderbilt, D. *Phys. Rev. B* **1997**, *56*, 12847.
(84) Berghold, G.; Mundy, C. J.; Romero, A. H.; Hutter, J.; Parrinello, M. *Phys. Rev. B* **2000**, *61*, 10040.
(85) Silvestrelli, P. L.; Marzari, N.; Vanderbilt, D.; Parrinello, M. *Solid State Commun.* **1998**, *107*, 7.
(86) Resta, R. *Phys. Rev. Lett.* **1998**, *80*, 1800.
(87) Resta, R.; Sorella, S. *Phys. Rev. Lett.* **1999**, *82*, 370.
(88) Putrino, A.; Sebastiani, D.; Parrinello, M. *J. Chem. Phys.* **2000**, *113*, 7102.
(89) Putrino, A.; Parrinello, M. *Phys. Rev. Lett.* **2002**, *88*, No. 176401.
(90) Borysow, J.; Moraldi, M.; Frommhold, L. *Mol. Phys.* **1985**, *56*, 913.
(91) Berne, B. J.; Pecora, R. *Dynamic light scattering: with applications to chemistry, biology, and physics*; R. E. Krieger Pub. Co.: Malabar, FL, 1990.
(92) Goncharov, A. F.; Struzhkin, V. V.; Mao, H. K.; Hemley, R. J. *Phys. Rev. Lett.* **1999**, *83*, 1998.
(93) Wernet, P.; Nordlund, D.; Bergmann, U.; Cavalleri, M.; Odelius, M.; Ogasawara, H.; Naslund, L. A.; Hirsch, T. K.; Ojamae, L.; Glatzel, P.; Pettersson, L. G. M.; Nilsson, A. *Science* **2004**, *304*, 995.
(94) Smith, J. D.; Cappa, C. D.; Wilson, K. R.; Messer, B. M.; Cohen, R. C.; Saykally, R. J. *Science* **2004**, *306*, 851.
(95) Wilson, K. R.; Schaller, R. D.; Co, D. T.; Saykally, R. J.; Rude, B. S.; Catalano, T.; Bozek, J. D. *J. Chem. Phys.* **2002**, *117*, 7738.
(96) Wilson, K. R.; Cavalleri, M.; Rude, B. S.; Schaller, R. D.; Nilsson, A.; Pettersson, L. G. M.; Goldman, N.; Catalano, T.; Bozek, J. D.; Saykally, R. J. *J. Phys.: Condens. Matter* **2002**, *14*, L221.
(97) Stohr, J. *NEXAFS Spectroscopy*; Springer Velag: Berlin, 2003.
(98) Myneni, S.; Luo, Y.; Naslund, L. A.; Cavalleri, M.; Ojamae, L.; Ogasawara, H.; Pelmenschikov, A.; Wernet, P.; Vaterlein, P.; Heske, C.; Hussain, Z.; Pettersson, L. G. M.; Nilsson, A. *J. Phys.: Condens. Matter* **2002**, *14*, L213.
(99) Cavalleri, M.; Odelius, M.; Nilsson, A.; Pettersson, L. G. M. *J. Chem. Phys.* **2004**, *121*, 10065.
(100) Triguero, L.; Pettersson, L. G. M.; Agren, H. *Phys. Rev. B* **1998**, *58*, 8097.
(101) Triguero, L.; Pettersson, L. G. M.; Agren, H. *J. Phys. Chem. A* **1998**, *102*, 10599.
(102) Slater, J. C.; Johnsson, K. H. *Phys. Rev. B* **1972**, *5*, 844.
(103) Hetenyi, B.; De Angelis, F.; Giannozzi, P.; Car, R. *J. Chem. Phys.* **2001**, *115*, 5791.
(104) Hetenyi, B.; De Angelis, F.; Giannozzi, P.; Car, R. *J. Chem. Phys.* **2004**, *120*, 8632.
(105) Cavalleri, M.; Odelius, M.; Nordlund, D.; Nilsson, A.; Pettersson, L. G. M. *Phys. Chem. Chem. Phys.* **2005**, *7*, 2854−2858.
(106) Bussolin, G.; Casassa, S.; Pisani, C.; Ugliengo, P. *J. Chem. Phys.* **1998**, *108*, 9516.
(107) Casassa, S. *Chem. Phys. Lett.* **2000**, *321*, 1.
(108) Casassa, S.; Pisani, C. *J. Chem. Phys.* **2002**, *116*, 9856.
(109) Casassa, S.; Ugliengo, P.; Pisani, C. *J. Chem. Phys.* **1997**, *106*, 8030.
(110) Liu, Z. F.; Siu, C. K.; Tse, J. S. *Chem. Phys. Lett.* **1999**, *309*, 335.
(111) Mantz, Y. A.; Geiger, F. M.; Molina, L. T.; Molina, M. J.; Trout, B. L. *J. Chem. Phys.* **2000**, *113*, 10733.
(112) Mantz, Y. A.; Geiger, F. M.; Molina, L. T.; Molina, M. J.; Trout, B. L. *Chem. Phys. Lett.* **2001**, *348*, 285.
(113) Mantz, Y. A.; Geiger, F. M.; Molina, L. T.; Molina, M. J.; Trout, B. L. *J. Phys. Chem. A* **2002**, *106*, 6972.
(114) Mantz, Y. A.; Geiger, F. M.; Molina, L. T.; Trout, B. L. *J. Phys. Chem. A* **2001**, *105*, 7037.
(115) Poshusta, R. D.; Tseng, D. C.; Hess, A. C.; McCarthy, M. I. *J. Phys. Chem.* **1993**, *97*, 7295.

(116) Svanberg, M.; Pettersson, J. B. C.; Bolton, K. *J. Phys. Chem. A* **2000**, *104*, 5787.
(117) Toth, G. *J. Phys. Chem. A* **1997**, *101*, 8871.
(118) Cicerone, R. J. *Science* **1987**, *237*, 35.
(119) Molina, M. J.; Tso, T. L.; Molina, L. T.; Wang, F. C. Y. *Science* **1987**, *238*, 1253.
(120) Solomon, S.; Garcia, R. R.; Rowland, F. S.; Wuebbles, D. J. *Nature* **1986**, *321*, 755.
(121) Tolbert, M. A.; Rossi, M. J.; Golden, D. M. *Science* **1988**, *240*, 1018.
(122) Tolbert, M. A.; Rossi, M. J.; Malhotra, R.; Golden, D. M. *Science* **1987**, *238*, 1258.
(123) Lee, S. H.; Leard, D. C.; Zhang, R. Y.; Molina, L. T.; Molina, M. J. *Chem. Phys. Lett.* **1999**, *315*, 7.
(124) Bianco, R.; Gertner, B. J.; Hynes, J. T. *Phys. Chem. Chem. Phys.* **1998**, *102*, 518.
(125) Bianco, R.; Hynes, J. T. *J. Phys. Chem. A* **1998**, *102*, 309.
(126) Bianco, R.; Hynes, J. T. *Int. J. Quantum Chem.* **1999**, *75*, 683.
(127) Bianco, R.; Hynes, J. T. *J. Phys. Chem. A* **1999**, *103*, 3797.
(128) Bianco, R.; Hynes, J. T. *J. Phys. Chem. A* **2003**, *107*, 5253.
(129) Bianco, R.; Thompson, W. H.; Morita, A.; Hynes, J. T. *J. Phys. Chem. A* **2001**, *105*, 3132.
(130) Bolton, K. *J. Mol. Struct.* **2003**, *632*, 145.
(131) Bolton, K.; Pettersson, J. B. C. *J. Am. Chem. Soc.* **2001**, *123*, 7360.
(132) Bournel, F.; Mangeney, C.; Tronc, M.; Laffon, C.; Parent, P. *Phys. Rev. B* **2002**, *65*, No. 201404.
(133) Devlin, J. P.; Uras, N.; Sadlej, J.; Buch, V. *Nature* **2002**, *417*, 269.
(134) Graham, J. D.; Roberts, J. T. *J. Phys. Chem.* **1994**, *98*, 5974.
(135) Graham, J. D.; Roberts, J. T. *Geophys. Res. Lett.* **1995**, *22*, 251.
(136) Horn, A. B.; Sodeau, J. R.; Roddis, T. B.; Williams, N. A. *J. Phys. Chem. A* **1998**, *102*, 6107.
(137) Kang, H.; Shin, T. H.; Park, S. C.; Kim, I. K.; Han, S. J. *J. Am. Chem. Soc.* **2000**, *122*, 9842.
(138) Milet, A.; Struniewicz, C.; Moszynski, R.; Sadlej, J.; Kisiel, Z.; Bialkowska-Jaworska, E.; Pszczolkowski, L. *Chem. Phys.* **2001**, *271*, 267.
(139) Re, S.; Osamura, Y.; Suzuki, Y.; Schaefer, H. F. *J. Chem. Phys.* **1998**, *109*, 973.
(140) Shevkunov, S. V. *Colloid J.* **2004**, *66*, 506.
(141) Shevkunov, S. V. *Colloid J.* **2004**, *66*, 230.
(142) Toubin, C.; Picaud, S.; Hoang, P. N. M.; Girardet, C.; Demirdjian, B.; Ferry, D.; Suzanne, J. *J. Chem. Phys.* **2002**, *116*, 5150.
(143) Banham, S. F.; Sodeau, J. R.; Horn, A. B.; McCoustra, M. R. S.; Chesters, M. A. *J. Vac. Sci. Technol. A* **1996**, *14*, 1620.
(144) Xu, S. C. *J. Chem. Phys.* **1999**, *111*, 2242.
(145) Donsig, H. A.; Herridge, D.; Vickerman, J. C. *J. Phys. Chem. A* **1998**, *102*, 2302.
(146) Donsig, H. A.; Herridge, D.; Vickerman, J. C. *J. Phys. Chem. A* **1999**, *103*, 9211.
(147) Donsig, H. A.; Vickerman, J. C. *J. Chem. Soc., Faraday Trans.* **1997**, *93*, 2755.
(148) Pursell, C. J.; Zaidi, M.; Thompson, A.; Fraser-Gaston, C.; Vela, E. *J. Phys. Chem. A* **2000**, *104*, 552.
(149) Ando, K.; Hynes, J. T. *Adv. Chem. Phys.* **1999**, *110*, 381.
(150) Ando, K.; Hynes, J. T. *J. Phys. Chem. A* **1999**, *103*, 10398.
(151) Leu, M. T.; Timonen, R. S.; Keyser, L. F. *J. Phys. Chem. A* **1997**, *101*, 278.
(152) Parent, P.; Laffon, C. *J. Phys. Chem. B* **2005**, *109*, 1547.
(153) Delzeit, L.; Rowland, B.; Devlin, J. P. *J. Phys. Chem.* **1993**, *97*, 10312.
(154) Andersson, P. U.; Nagard, M. B.; Pettersson, J. B. C. *J. Phys. Chem. B* **2000**, *104*, 1596.
(155) Uras, N.; Rahman, M.; Devlin, J. P. *J. Phys. Chem. B* **1998**, *102*, 9375.
(156) Sadtchenko, V.; Giese, C. F.; Gentry, W. R. *J. Phys. Chem. B* **2000**, *104*, 9421.
(157) Furukawa, Y.; Nada, H. *J. Phys. Chem. B* **1997**, *101*, 6167.
(158) Furukawa, Y.; Yamamoto, M.; Kuroda, T. *J. Cryst. Growth* **1987**, *82*, 665.
(159) Karim, O. A.; Haymet, A. D. J. *Chem. Phys. Lett.* **1987**, *138*, 531.
(160) Karim, O. A.; Haymet, A. D. J. *J. Chem. Phys.* **1988**, *89*, 6889.
(161) Nada, H.; Furukawa, Y. *Appl. Surf. Sci.* **1997**, *121*, 445.
(162) Nada, H.; Furukawa, Y. *Surf. Sci.* **2000**, *446*, 1.
(163) Clary, D. C.; Wang, L. C. *J. Chem. Soc., Faraday Trans.* **1997**, *93*, 2763.
(164) Packer, M. J.; Clary, D. C. *J. Phys. Chem.* **1995**, *99*, 14323.
(165) Wang, L. C.; Clary, D. C. *J. Chem. Phys.* **1996**, *104*, 5663.
(166) Kroes, G. J.; Clary, D. C. *J. Phys. Chem.* **1992**, *96*, 7079.
(167) Xantheas, S. S.; Dang, L. X. *J. Phys. Chem.* **1996**, *100*, 3989.
(168) Petrenko, V. F.; Whitworth, R. W. *Physics of Ice*; Oxford University Press: New York, 1999.
(169) Molina, M. J. *Chemistry of the Atmosphere: Its Impact on Global Change*; Blackwell Scientific Publications: Oxford, U.K., 1994.
(170) Bullemer, B.; Riehl, N. *Solid State Commun.* **1966**, *4*, 447.
(171) Dosch, H.; Lied, A.; Bilgram, J. H. *Surf. Sci.* **1995**, *327*, 145.
(172) Gilpin, R. R. *J. Colloid Interface Sci.* **1980**, *77*, 435.
(173) Golecki, I.; Jaccard, C. *J. Phys. C: Solid State Phys.* **1978**, *11*, 4229.
(174) Mazzega, E.; Pennino, U. D.; Loria, A.; Mantovani, S. *J. Chem. Phys.* **1976**, *64*, 1028.
(175) Mizuno, Y.; Hanafusa, N. *J. Phys.* **1987**, *48*, 511.
(176) Nason, D.; Fletcher, N. H. *J. Chem. Phys.* **1975**, *62*, 4444.
(177) Abbatt, J. P. D.; Molina, M. J. *J. Phys. Chem.* **1992**, *96*, 7674.
(178) Hoover, W. G. *Phys. Rev. A* **1985**, *31*, 1695.
(179) Nose, S. *J. Chem. Phys.* **1984**, *81*, 511.
(180) Martyna, G. J.; Klein, M. L.; Tuckerman, M. *J. Chem. Phys.* **1992**, *97*, 2635.
(181) McGrath, M. J.; Siepmann, J. I.; Kuo, I. F. W.; Mundy, C. J.; VandeVondele, J.; Sprik, M.; Hutter, J.; Mohamed, F.; Krack, M.; Parrinello, M. *Comput. Phys. Commun.* **2005**, *169*, 289.
(182) McGrath, M. J.; Siepmann, J. I.; Kuo, I. F. W.; Mundy, C. J.; VandeVondele, J.; Hutter, J.; Mohamed, F.; Krack, M. *J. Phys. Chem. A* **2006**, *110*, 640.
(183) Kroes, G. J. *Surf. Sci.* **1992**, *275*, 365.
(184) Schaff, J. E.; Roberts, J. T. *J. Phys. Chem.* **1994**, *98*, 6900.
(185) Allouche, A.; Couturier-Tamburelli, I.; Chiavassa, T. *J. Phys. Chem. B* **2000**, *104*, 1497.
(186) Kresse, G.; Hafner, J. *Phys. Rev. B* **1993**, *47*, 558.
(187) Kresse, G.; Hafner, J. *Phys. Rev. B* **1994**, *49*, 14251.
(188) Laasonen, K.; Sprik, M.; Parrinello, M.; Car, R. *J. Chem. Phys.* **1993**, *99*, 9080.
(189) Sprik, M.; Hutter, J.; Parrinello, M. *J. Chem. Phys.* **1996**, *105*, 1142.
(190) Asthagiri, D.; Pratt, L. R.; Kress, J. D. *Phys. Rev. E* **2003**, *68*, No. 041505.
(191) Sullivan, D. M.; Bagchi, K.; Tuckerman, M. E.; Klein, M. L. *J. Phys. Chem. A* **1999**, *103*, 8678.
(192) Finlayson-Pitts, B. J. *Chem. Rev.* **2003**, *103*, 4801.
(193) Vieceli, J.; Roeselova, M.; Tobias, D. J. *Chem. Phys. Lett.* **2004**, *393*, 249.
(194) Chuang, P. Y.; Charlson, R. J.; Seinfeld, J. H. *Nature* **1997**, *390*, 594.
(195) Morita, A.; Sugiyama, M.; Kameda, H.; Koda, S.; Hanson, D. R. *J. Phys. Chem. B* **2004**, *108*, 9111.
(196) Wilson, K. R.; Tobin, J. G.; Ankudinov, A. L.; Rehr, J. J.; Saykally, R. J. *Phys. Rev. Lett.* **2000**, *85*, 4289.
(197) Wilson, K. R.; Rude, B. S.; Catalano, T.; Schaller, R. D.; Tobin, J. G.; Co, D. T.; Saykally, R. J. *J. Phys. Chem. B* **2001**, *105*, 3346.
(198) Richmond, G. L. *Chem. Rev.* **2002**, *102*, 2693.
(199) Raymond, E. A.; Richmond, G. L. *J. Phys. Chem. B* **2004**, *108*, 5051.
(200) Raymond, E. A.; Tarbuck, T. L.; Brown, M. G.; Richmond, G. L. *J. Phys. Chem. B* **2003**, *107*, 546.
(201) Allen, H. C.; Raymond, E. A.; Richmond, G. L. *Curr. Opin. Colloid Interface Sci.* **2000**, *5*, 74.
(202) Du, Q.; Superfine, R.; Freysz, E.; Shen, Y. R. *Phys. Rev. Lett.* **1993**, *70*, 2313.
(203) Schnitzer, C.; Baldelli, S.; Campbell, D. J.; Shultz, M. J. *J. Phys. Chem. A* **1999**, *103*, 6383.
(204) Schnitzer, C.; Baldelli, S.; Shultz, M. J. *J. Phys. Chem. B* **2000**, *104*, 585.
(205) Liu, D. F.; Ma, G.; Levering, L. M.; Allen, H. C. *J. Phys. Chem. B* **2004**, *108*, 2252.
(206) Wilson, K. R.; Cavalleri, M.; Rude, B. S.; Schaller, R. D.; Catalano, T.; Nilsson, A.; Saykally, R. J.; Pettersson, L. G. M. *J. Phys. Chem. B* **2005**, *109*, 10194.
(207) Townsend, R. M.; Gryko, J.; Rice, S. A. *J. Chem. Phys.* **1985**, *82*, 4391.
(208) Townsend, R. M.; Rice, S. A. *J. Chem. Phys.* **1991**, *94*, 2207.
(209) Wilson, M. A.; Pohorille, A.; Pratt, L. R. *J. Phys. Chem.* **1987**, *91*, 4873.
(210) Benjamin, I. *J. Chem. Phys.* **1991**, *95*, 3698.
(211) Benjamin, I. *Phys. Rev. Lett.* **1994**, *73*, 2083.
(212) Schnitzer, C.; Baldelli, S.; Shultz, M. J. *Chem. Phys. Lett.* **1999**, *313*, 416.
(213) Vassilev, P.; Hartnig, C.; Koper, M. T. M.; Frechard, F.; van Santen, R. A. *J. Chem. Phys.* **2001**, *115*, 9815.
(214) Marx, D. *Science* **2004**, *303*, 634.
(215) Kuo, I. F. W.; Mundy, C. J. *Science* **2004**, *303*, 658.
(216) Gerstein, M.; Tsai, J.; Levitt, M. *J. Mol. Biol.* **1995**, *249*, 955.
(217) Harpaz, Y.; Gerstein, M.; Chothia, C. *Structure* **1994**, *2*, 641.
(218) Modig, K.; Pfrommer, B. G.; Halle, B. *Phys. Rev. Lett.* **2003**, *90*, No. 075502.
(219) Hunt, P.; Sprik, M.; Vuilleumier, R. *Chem. Phys. Lett.* **2003**, *376*, 68.
(220) Vuilleumier, R.; Sprik, M. *J. Chem. Phys.* **2001**, *115*, 3454.
(221) Reuter, K.; Frenkel, D.; Scheffler, M. *Phys. Rev. Lett.* **2004**, *93*, No. 116105.
(222) Kumar, S.; Bouzida, D.; Swendsen, R. H.; Kollman, P. A.; Rosenberg, J. M. *J. Comput. Chem.* **1992**, *13*, 1011.

(223) Kumar, S.; Rosenberg, J. M.; Bouzida, D.; Swendsen, R. H.; Kollman, P. A. *J. Comput. Chem.* **1995**, *16*, 1339.
(224) Souaille, M.; Roux, B. *Comput. Phys. Commun.* **2001**, *135*, 40.
(225) Bolhuis, P. G.; Chandler, D.; Dellago, C.; Geissler, P. L. *Annu. Rev. Phys. Chem.* **2002**, *53*, 291.
(226) Voter, A. F. *Phys. Rev. Lett.* **1997**, *78*, 3908.
(227) Henkelman, G.; Johannesson, G.; Jonsson, H. In *Theoretical methods in condensed phase chemistry*; Schwartz, S. D., Ed.; Progress in Theoretical Chemistry and Physics, Vol. 5; Kluwar Academic Publishers: Dordrecht, The Netherlands, 2000.
(228) Zhu, Z. W.; Tuckerman, M. E.; Samuelson, S. O.; Martyna, G. J. *Phys. Rev. Lett.* **2002**, *88*, No. 100201.
(229) VandeVondele, J.; Rothlisberger, U. *J. Phys. Chem. B* **2002**, *106*, 203.
(230) Laio, A.; Parrinello, M. *Proc. Natl. Acad. Sci. U.S.A.* **2002**, *99*, 12562.
(231) Geissler, P. L.; Dellago, C.; Chandler, D.; Hutter, J.; Parrinello, M. *Science* **2001**, *291*, 2121.
(232) Iannuzzi, M.; Laio, A.; Parrinello, M. *Phys. Rev. Lett.* **2003**, *90*, No. 238302.
(233) Stirling, A.; Iannuzzi, M.; Laio, A.; Parrinello, M. *ChemPhysChem* **2004**, *5*, 1558.
(234) Stirling, A.; Iannuzzi, M.; Parrinello, M.; Molnar, F.; Bernhart, V.; Luinstra, G. A. *Organometallics* **2005**, *24*, 2533.
(235) Iannuzzi, M.; Parrinello, M. *Phys. Rev. Lett.* **2004**, *93*, No. 025901.
(236) Gervasio, F. L.; Laio, A.; Iannuzzi, M.; Parrinello, M. *Chem.—Eur. J.* **2004**, *10*, 4846.
(237) Churakov, S. V.; Iannuzzi, M.; Parrinello, M. *J. Phys. Chem. B* **2004**, *108*, 11567.
(238) Martonak, R.; Laio, A.; Bernasconi, M.; Ceriani, C.; Raiteri, P.; Zipoli, F.; Parrinello, M. *Z. Kristallogr.* **2005**, *220*, 489.
(239) Gervasio, F. L.; Laio, A.; Parrinello, M. *J. Am. Chem. Soc.* **2005**, *127*, 2600.
(240) Martonak, R.; Laio, A.; Parrinello, M. *Phys. Rev. Lett.* **2003**, *90*, No. 075503.
(241) Ceccarelli, M.; Danelon, C.; Laio, A.; Parrinello, M. *Biophys. J.* **2004**, *87*, 58.
(242) Micheletti, C.; Laio, A.; Parrinello, M. *Phys. Rev. Lett.* **2004**, *92*, No. 170601.
(243) Laio, A.; Rodriguez-Fortea, A.; Gervasio, F. L.; Ceccarelli, M.; Parrinello, M. *J. Phys. Chem. B* **2005**, *109*, 6714.
(244) Ensing, B.; Laio, A.; Parrinello, M.; Klein, M. L. *J. Phys. Chem. B* **2005**, *109*, 6676.
(245) Ensing, B.; Laio, A.; Gervasio, F. L.; Parrinello, M.; Klein, M. L. *J. Am. Chem. Soc.* **2004**, *126*, 9492.
(246) Jorgensen, W. L.; Chandrasekhar, J.; Madura, J.; Impey, R. W.; Klein, M. L. *J. Chem. Phys.* **1983**, *79*, 926.
(247) Hunt, P.; Sprik, M.; Vuilleumier, R. *Chem. Phys. Lett.* **2003**, *376*, 68.

CR040375T